Fracture unclogging: A numerical study of seismically induced viscous shear stresses in fluid-saturated fractured rocks

Nicolás D. Barbosa[1], Jürg Hunziker[2], Simón Lissa[2], Erik H. Saenger[3], and Matteo Lupi[1].

[1]Department of Earth Sciences, University of Geneva, Geneva, Switzerland
[2]Institute of Earth Sciences, University of Lausanne, Lausanne, Switzerland
[3]International Geothermal Centre and Ruhr-Universität, Bochum, Germany

*

Key Points:

- We compute viscous shear stresses in fluid-saturated fractures in response to the dynamic strain of body waves
- We analyze fracture unclogging potential in terms of the seismic wave, the rock, the saturating fluid, and the fracture network properties
- Seismically-induced fracture unclogging is plausible for typical seismic strains and frequencies

Corresponding author: N. B. Barbosa, `nicolas.barbosa@unige.ch`
*Accepted for publication in JGR: Solid Earth.

Abstract

Dynamic shaking imposed by passing seismic waves is able to promote various hydrological processes in fractured reservoirs. This is often associated with seismically-induced fracture unclogging due to mobilization of deposited colloids in the fracture network which, in turn, affects permeability at the reservoir scale. Numerous laboratory and field studies pointed out that fracture unclogging can be initiated when viscous shear stresses in the fracture fluid are in the range of 0.1-1 Pascals. In this numerical study, we compute viscous shear stress in a fluid-saturated fractured medium due to the action of passing P- and S-waves. We perform a sensitivity analysis in terms of fluid, fracture, and host rock physical properties as well as seismic wave characteristics. Our results show that seismically-induced viscous shearing increases with frequency and seismic strain and can be in the order of those initiating fracture unclogging for typical seismic strains and frequencies. S-waves tend to produce viscous shearing approximately two times larger than P-waves and, for anisotropic distribution of fractures, it is extremely dependent on the direction of wave propagation. Moreover, larger viscous shearing is expected for more viscous fluids and stiffer host rocks. Regarding the fracture network distribution, for the same fracture density, the presence of longer fractures drastically increases the potential of fracture unclogging at seismic frequencies. The fracture aperture distribution, on the other hand, can also affect the development of viscous shearing. Fractures with correlated distributions of contact areas exhibit an order of magnitude larger viscous shearing than uncorrelated ones.

1 Introduction

For any given scale, fractures dominate the mechanical properties of reservoirs as well as their hydraulic characteristics. In Earth Sciences and in particular in reservoir characterization, fractures are key features affecting fluid flow and may determine whether reservoirs are economically exploitable or not. The hydraulic conductivity of a reservoir is a transient property (Borg et al., 1976; Ameli et al., 2014; Pyrak-Nolte & Nolte, 2016). Hydraulic stimulation is arguably one of the most effective methods to increase the hydraulic conductivity of a reservoir (Economides & Nolte, 1989). However, the permeability of reservoirs may also be increased by the mobilization of colloids at the pore scale through pre-existing fractures (Elkhoury et al., 2011). Colloids are commonly defined as fine particles between 1 nm and 10 μm whose nature can be either inorganic (e.g., mineral precipitates) or organic (e.g., bacteria). When a colloidal particle travels through a fluid-saturated fracture it is affected by several processes among which the most important are adsorption, desorption, physical straining, gravity settling, and diffusion into the rock matrix (W. Zhang et al., 2012). Some of these processes promote collisions between colloids and the fracture walls, which once established can favor further attachment of additional particles ultimately reducing the hydraulic conductivity of the fracture in a process commonly referred to as fracture clogging. When hydrodynamic drag forces overcome the adhesive forces, colloidal desorption or detachment from fracture surfaces can be initiated (Bergendahl & Grasso, 2000) leading to an enhancement of the overall hydraulic conductivity (fracture unclogging). In this work, we investigate the ability of body waves travelling across a fluid-saturated fractured medium to produce transient drag forces in the fluid. In particular, we explore under which conditions, seismically-induced viscous shear stresses are capable of initiating fracture unclogging.

Direct observations of colloidal mobilization due to transient stimulation were conducted at the meso-scale (i.e. tens of meters). As an example, a two-year-long monitoring study at the Grimsel Test Site, Switzerland, showed that fracture fluids in crystalline rocks transported inorganic colloids at concentrations of about 10^{10} particles per liter (Degueldre et al., 1989). Micro-seismicity and variations in the groundwater flow rate were the most likely reasons for the detachment of colloids. At the regional scale, field data pointed out seismically-induced fracture unclogging due to colloidal mobilization (Manga et al. (2012) and references therein). Although no dedicated experiments investigated colloidal mobilization, it has been recognized as a mechanism of permeability enhancement that could explain a number of hydrological and hydrogeological responses to distant earthquakes (Rojstaczer et al., 1995). Field observations showed that passing seismic waves affected stream-flow and spring discharge (Manga et al., 2003), groundwater level (Brodsky et al., 2003; Elkhoury et al., 2006; Kocharyan et al., 2011; Xue et al., 2013; Y. Zhang et al., 2015; Shi et al., 2019), oil wells production (Beresnev & Johnson, 1994; Mirzaei-Paiaman & Nourani, 2012) temperature and composition of groundwater (Mogi et al., 1989), seismicity at geothermal systems (Lupi, Fuchs, & Saenger, 2017), eruption of mud volcanoes (Rudolph & Manga, 2010; Lupi et al., 2013), and liquefaction of unconsolidated sediments (C.-Y. Wang, 2007). Mogi et al. (1989) argued that the observed increase of geothermal flux and turbidity in an artesian spring at the Usami Hot Springs, Japan, after the passage of seismic waves was related to the mobilization of colloids at the pore scale. Brodsky et al. (2003) proposed a model to explain water level changes in wells based on the unclogging of highly conductive fractures due to the rapid flow induced by seismic surface waves. Brodsky et al. (2003) showed that the seismically-induced fracture unclogging is a function of the frequency and amplitude of the dynamic strain imposed by the passing seismic waves. By measuring permeability from water well level changes in response to solid Earth tides, Elkhoury et al. (2006) found that permeability in a fractured rock system was significantly increased (up to three times) after the passage of seismic waves from regional earthquakes. Their data indicated that the permeability increases, which were approximately linearly related to the dynamic strains, were followed by a slow permeability recovery to the pre-seismic stress state. The latter is a common observation usually evoked to support the fracture unclogging mechanism as the recovery is believed to be related to the subsequent clogging of fractures (Kocharyan et al., 2011; Candela et al., 2014).

Permeability increases promoted by passing seismic waves are particularly effective in geological systems characterized by elevated pore pressures at depth (Manga & Brodsky, 2006; Farías et al., 2014). This is the case in geothermal systems or in geological settings where isolated compartments of high pressure fluids may develop at depth. The subsequent redistribution of the pore fluid pressure may, in turn, cause permanent changes in the mechanical and hydraulic properties at depth (Kocharyan et al., 2011). In this sense, C.-Y. Wang (2007) argued that enhanced permeability may bridge hydraulically isolated regions characterised by high pore pressure and low liquefaction potential to regions more prone to liquefaction. Several studies (Hill, 2008; Saccorotti et al., 2013; Lupi, Fuchs, & Saenger, 2017) have shown that dynamic stresses imposed by a passing seismic wave in the order of a few kPa can be sufficient to destabilize critically loaded faults by increasing their pore fluid pressure. In this scenario, the permeability increase due to the seismically-induced unclogging of fine particles may accelerate the diffusion of pore pressure into faults, decreasing the confining effective normal stress ultimately prompting the system to failure. Although dynamic triggering effects are typically associated with the seismic energy of surface waves generated by teleseismic events (Brodsky et al., 2003; Brodsky & Prejean, 2005; Elkhoury et al., 2011), it has been shown that body waves released from regional earthquakes can have a similar impact on a variety of fluid-saturated systems (C.-y. Wang et al., 2009; Lupi et al., 2013, 2015; Lupi, Frehner, et al., 2017). The effects of body waves can be even more important than those related to surface waves in geological settings (e.g. anticlines and piercement structures) focusing and amplifying the incoming seismic energy (Lupi, Frehner, et al., 2017).

The physics of the changes of hydraulic conductivity of fractured media due to transient pressure changes has been investigated mostly via laboratory experiments. These are summarised in section 2 and reported in Table 1. During laboratory experiments, pore pressure (or stress) oscillations are imposed on intact or fractured fluid-saturated rock samples to investigate transient variations of effective permeability. In general, the permeability changes are found to be consistent with the mobilization of trapped colloidal particles. During the shaking, the development of viscous shear forces in the fluid removes colloids blocking flow paths thus changing the fracture internal structure and consequently their hydraulic properties (Liu & Manga, 2009). After the transient stimulation is ceased, the permeability recovery of the sample related to the progressive reclogging of the pores and fractures is investigated.

The viscous shear stress tensor components τ_{ij}, caused by the motion of a viscous fluid are defined as (Kutay & Aydilek, 2009)

$$\tau_{ij} = \eta\left(\frac{\partial v_i}{\partial x_j} + \frac{\partial v_j}{\partial x_i}\right), \qquad i, j = x, y, z, \tag{1}$$

where η is the fluid viscosity and v_j is the $j-$component of the fluid velocity. From Eq. 1 it follows that high velocity gradients generated due to the presence of large local pressure gradients directly affect the magnitude of the viscous shear stress acting on the fluid-solid interface. In order to evaluate the plausibility of colloid mobilization as a mechanism for seismically driven permeability changes, Manga et al. (2012) compared observations of mobilization with the viscous shear stress that is being applied to the colloidal deposits. They found that shear stresses of 0.1-1 Pa appear to be sufficient to initiate colloidal mobilization in a wide range of systems. These relatively low values of viscous shearing further support colloid mobilization as a plausible mechanism for some of the commonly observed hydrogeological responses to dynamic stresses. Furthermore, Manga et al. (2012) pointed out that the computed values may represent a conservative threshold as the consequences of permeability changes had to be large enough to be detectable.

Field (Brodsky et al., 2003; C.-y. Wang et al., 2009), laboratory (Bergendahl & Grasso, 2000; Li et al., 2005; Chen et al., 2018), and theoretical studies (Bai & Tien, 1997; Kutay & Aydilek, 2009) converge in showing that the removal efficiency of particles from poroelastic materials is correlated with the viscous shear stress in the fluid driven by pore pressure oscillations. Hence, investigating the behavior of seismically-induced viscous shear stresses in fractured fluid-saturated systems is key to understand permeability changes driven by colloidal mobilization. However, despite the recent analytical (Brodsky et al., 2003), field (Taira et al., 2018), and experimental (Candela et al., 2014) studies supporting the wave-induced fracture unclogging mechanism, to the best of our knowledge, there is a lack of numerical studies investigating such processes. In this work, we explore which seismic wave characteristics favor the development of viscous shearing that may be sufficient to initiate fracture unclogging via colloidal mobilization. In this regard, it is important to mention that although seismically-induced fracture unclogging may affect the fracture physical properties (e.g., fracture aperture), accounting for such effects and their corresponding evolution is beyond the scope of this study. In Section 2, we discuss the underlying mechanism of permeability enhancement including a brief review of pertinent laboratory experiments and a description of the conditions under which colloidal mobilization due to wave-induced viscous shearing can occur. In Section 3 we present our numerical strategy. In Section 4 the seismically-induced viscous shearing is analyzed as a function of the properties of the propagating wave (e.g., wave mode, frequency, direction of propagation) and the fractured rock (fracture, background rock, and fluid properties). In Section 5, we further discuss the limitations and implications of our study and summarize the most important results in the conclusions section.

2 Fracture unclogging mechanism

The magnitude of permeability changes caused by dynamic stresses (few kPa), is typically less than the changes caused by fracturing (few MPa) used to enhance reservoir permeability of about two orders of magnitude (Amann et al., 2018). The laboratory experiments listed in Table 1 investigated variations of the effective permeability of intact or fractured fluid-saturated rock samples upon imposing dynamic stresses similar or slightly larger than those created by solid Earth (10^{-3} MPa) or Ocean (10^{-2} MPa) tides and passing seismic waves.

Roberts (2005) imposed sinusoidal cycles of axial stress (refer to Table 1 for the frequencies and amplitudes) on fluid-saturated intact Berea sandstone samples. For low-amplitude oscillations, Roberts (2005) did not observe effective permeability variations. However, upon increasing the amplitude of the transient stress variations to 0.6 MPa and then to 0.9 MPa, permeability increased 15% and 20%, respectively. Permeability returned to pre-stimulation values over a period of 24 hours after the cycles were stopped. Liu and Manga (2009) performed oscillatory experiments on fractured water-saturated sandstone cores. The amplitude of the imposed axial stress was in the order of tens of kPa. Both permeability and sample size decreased after each set of oscillations. Liu and Manga (2009) speculated that this may have been due to a redistribution of fine particles in the fractures. The decrease resulted proportional to the cumulative amount of transient stress applied to the samples. Kocharyan et al. (2011) studied wave-induced fracture unclogging effects by measuring changes in the water flow rate through a fracture artificially clogged with fine corundum particles. In the experiment, the sample was subjected to the action of dynamic pulses produced by steel ball hits. During the stimulation, some of the particles were leached out when the flow rate drastically increased. After termination of the stimulation, gradual re-clogging and restoring of broken barriers made the effective permeability of the fracture to return to the initial values. Elkhoury et al. (2011) pointed out that imposing pore pressure oscillations in a fractured rock sample can change permeability up to 50% of its original value. As a direct indication of the colloidal mobilization, Elkhoury et al. (2011) found gouge aligned over the fracture surface, with increasing quantities in the downstream direction, after taking the samples out of the apparatus. More recently, Candela et al. (2014) applied the same method and investigated the evolution of permeability for intact and fractured rocks saturated with deionized water and brines with NaCl 25 wt%, NaCl 5 wt%, and $CaCl_2$ 5 wt%. These authors found permeability enhancement on both intact and fractured samples. Furthermore, the magnitude of permeability enhancement and the rate of permeability recovery was proportional to the ionic strength of the pore fluid. The range of permeability enhancement reported by Candela et al. (2014) was 1-60% for dynamic strain amplitudes ranging from $7{\times}10^{-7}$ to $7{\times}10^{-6}$. Candela et al. (2015) expanded on the experiments of Candela et al. (2014) to analyze the dependence of the permeability changes with the frequency of the oscillation. For a fractured Berea sandstone and pressure oscillation frequencies of 0.05, 0.2, and 1 Hz, Candela et al. (2015) observed average relative increases in permeability of 10%, 25%, and 70%, respectively.

The permeability changes recorded during the experiments listed in Table 1 were attributed to the fast flushing and gradual re-clogging of colloids at the pore space or between fracture asperities. Other possible mechanisms driving permeability changes in laboratory experiments include micro-fracturing and shearing of the rock samples (Ishibashi et al., 2018), fracture aperture changes (Liu & Manga, 2009), and differential poroelastic behavior of matrix and fractures (Faoro et al., 2012). Observations supporting the unclogging mechanism over other mechanisms are (1) recovery of the initial permeability after stimulation (i.e., reversible mechanism), (2) fractured samples have shown slightly higher direct permeability enhancement compared to intact samples (i.e., influence of preferential flow paths), and (3) absence of permanent deformation of the sample after stimulation ceases (except in Liu and Manga (2009)). The re-clogging of the fluid pathways cleared by the seismic shaking has been found to depend on a complex combination of the amount of permeability enhancement, the pore-space geometry, the flow rates, the ionic strength of the pore-fluid, the colloidal size distribution and concentration (Roberts & Abdel-Fattah, 2009; Elkhoury et al., 2011; Candela et al., 2014). Elkhoury et al. (2011) proposed an empirical relation in which the recovery of permeability in samples affected by oscillatory stresses occurs as t^{-p}, where t is the time and the exponent p can be in-

Table 1. Summary of key experiments investigating pores and fractures unclogging as a result of applying transient pressure changes to the sample. The table was extended from the review of Manga et al. (2012).

Authors	Frequency (Hz)	Amplitude	Oscillations	Samples	Permeability response	Recovery time
Roberts (2005)	50	0.3 - 0.9 MPa	Axial stress	Intact	Increase	24 hs
Liu and Manga (2009)	0.3 - 2.5	Strains 10^{-4}	Axial Displacement	Fractured	Decrease	No recovery
Elkhoury et al. (2011)	0.05	0.02 - 0.3 MPa	Pore pressure	Fractured	Increase	tens of minutes
Kocharyan et al. (2011)	Not documented	Strains 10^{-7} - 10^{-5}	Steel ball impacts	Fractured	Increase	tens of minutes
Candela et al. (2014)	0.05	0.01 - 0.5 MPa	Pore pressure	Fractured and intact	Increase	Several minutes
Candela et al. (2015)	0.05 - 1	0.14 - 0.5 MPa	Pore pressure	Fractured	Increase	Several minutes

terpreted as the inverse of the average flow dimension of the system. In the case of flow dominated by two-dimensional fractures, Elkhoury et al. (2011) found that $p = 1/2$.

In summary, the experimental literature described above points out that strain amplitudes of the order of 10^{-7}-10^{-5} are capable of affecting permeability which is in agreement with natural observations for seismic waves (Elkhoury et al., 2006; Lupi, Frehner, et al., 2017). Furthermore, the transient permeability enhancement due to fracture unclogging scales with the amplitude and frequency of the oscillatory strain (Elkhoury et al., 2011; Candela et al., 2014, 2015). In order to scale these observations to the field scale, in the following, we investigate the coupling between the imposed strains during the passage of seismic waves and the development of viscous shear forces in a fracture necessary to initiate the fracture unclogging.

3 Methodology

Colloidal mobilization promoted by viscous shearing is caused by seismic waves whose wavelengths can be much larger than the fracture-scale at which the process takes place (Brodsky et al., 2003). Due to the large difference of scales, the direct numerical simulation of seismically-induced fracture-scale processes is, in most cases, computationally challenging (Rubino et al., 2016). An effective approach for bridging such a scale gap consists in emulating the action of a propagating seismic wave through the application of oscillatory displacement fields on the boundaries of a representative elementary volume (REV) of the fractured formation (Fig. 1 arrow a). Given that the size of the REV, whose structure and seismic response is typical of the whole medium, can be much smaller than the dominant seismic wavelengths, it is possible to focus on sub-wavelength scale features and processes (e.g., viscous shearing at the walls of a fracture). This numerical upscaling approach is commonly used to infer effective seismic properties from the resulting strain-stress state of the sample (Rubino et al., 2013; Quintal et al., 2016). Here, we use it to calculate viscous shearing (τ_{ij}) in fluid-saturated fractured rocks due to the strains imposed by seismic waves with wavelengths larger than the size of the REV (Fig. 1 arrow b).

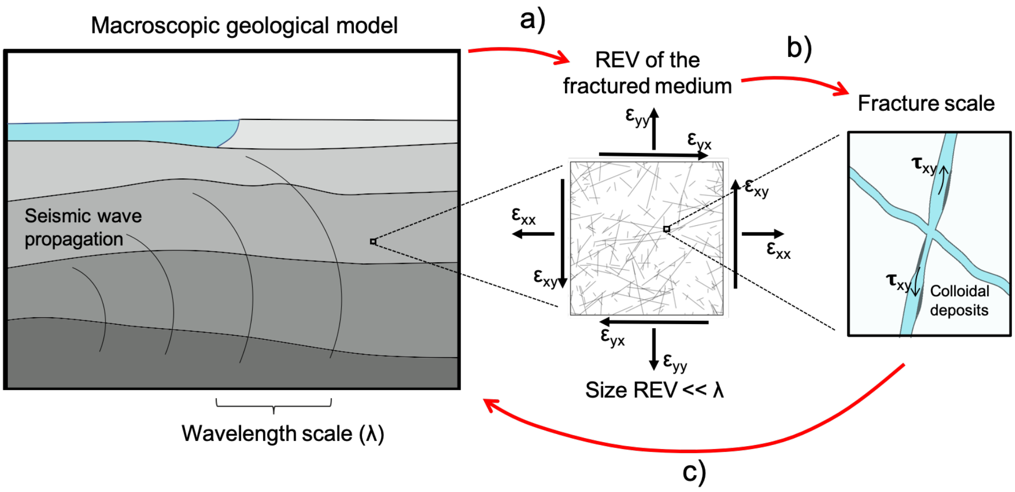

Figure 1. Schematic illustration of the methodology used to compute viscous shear stresses at the fracture scale. A propagating seismic wave imposes dynamic strains to the fractured formation, which we emulate by applying an oscillatory relaxation test to the REV of the formation (a). The dynamic strains produce pressure gradients and fluid motion inside the fractures, which are translated into viscous shear stresses (b). Viscous shearing applied to colloidal deposits can detach colloids from the fracture walls leading to changes in the overall hydraulic conductivity of the formation (c).

Rubino et al. (2013) showed that in the presence of hydraulically connected fractures, seismic waves may experience attenuation and velocity dispersion related to fluid pressure diffusion (FPD) within the fractures. The FPD occurs when the passing waves induce a fluid pressure gradient between connected fractures. During the corresponding fluid pressure equilibration, seismic energy is dissipated. In this work, we explore the link between the wave-induced FPD between connected fractures (FF-FPD) and the development of viscous shear stresses (Eq. 1) at the walls of the fractures (Fig. 1 arrow b). To do so, we use the procedure of Quintal et al. (2016) and apply a finite element technique to numerically solve a coupled system of equations stated in the space-frequency domain and consisting of the quasi-static linearized Navier-Stokes equation for the laminar flow of a compressible viscous fluid and the linear elastic equation for a nonporous solid material (Appendix A). This allows for modelling the associated spatial flow patterns inside the fractures (Quintal et al., 2016) from which the viscous shear stress can be obtained using Eq. 1. The methodology also reproduces the energy dissipation due to FF-FPD producing the frequency-dependent seismic wave attenuation and velocity dispersion observed by Rubino et al. (2013).

For the computation of the seismically-induced viscous shear stress in the fluid of the fractures, we first consider a simple 2D numerical model corresponding to an REV of a periodically fractured medium (Fig. 2). The 2D problem that we tackle is equivalent to a 3D case under plane strain conditions (where no strain outside the modelling plane is allowed to develop). We refer as x and y to the orthogonal directions in the modelling plane (Fig. 2) while z is the direction perpendicular to the $x-y$ plane. It follows that the only non-zero component of the viscous shear stress tensor is τ_{xy}. Despite the 2D nature of the simulations, it allows to examine the dependence of τ_{xy} on different seismic wave characteristics (i.e., wave mode, frequency, direction of propagation), fractured rock (e.g., host rock stiffness, fracture network distributions), and fluid properties. Once

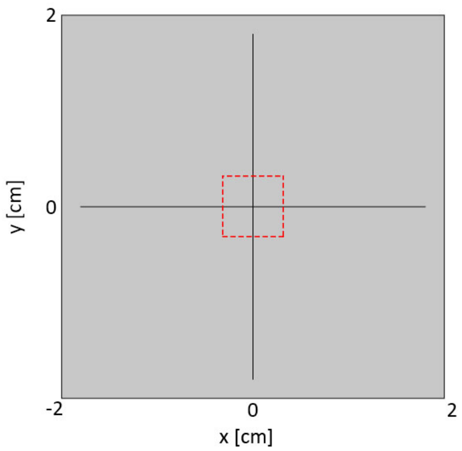

Figure 2. Synthetic sample representing a unit cell of a periodically fractured rock containing two connected orthogonal fluid-saturated fractures. The background is assumed to be elastic and the fractures are saturated with a viscous fluid. The corresponding physical properties are given in Table 2. The aspect ratio of the fractures is 2.77×10^{-4}. The red dashed square illustrates the region of the model shown in Fig. 4.

this sensitivity analysis is performed, a 3D fractured model is presented at the end of section 4.

The fractures of Fig. 2 are filled with a compressible viscous fluid, whereas the embedding background medium is described by the properties of an elastic solid. The fluid properties considered in this work correspond to water and brine at ambient pressure and temperature conditions (see Table 2), similar to those used in the laboratory experiments described in Section 2. We assume that the background rock hosting the fractures is modelled as a nonporous elastic medium while fractures are fluid-filled voids of arbitrary shape. This modelling implies that the fractures are hydraulically isolated from the surrounding background and thus FPD can only occur within the fractures.

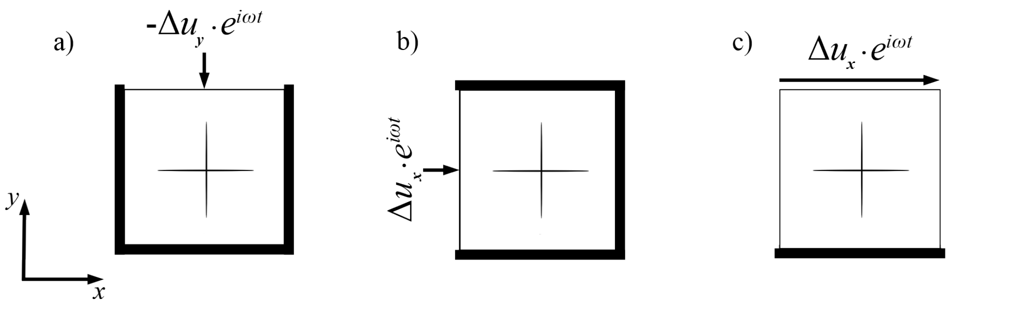

Figure 3. Numerical oscillatory relaxation tests. Panels a), b), and c) show the imposed boundary conditions for the vertical, horizontal, and shear relaxation tests, respectively. Vertical and horizontal relaxation tests simulate the action of a normally (perpendicular to the x-axis) and horizontally (parallel to the x-axis) incident P-wave. The shear relaxation test simulates the action of normally incident S-wave.

To compute the effects of FPD between hydraulically connected fractures due to the action of seismic waves at different incidence angles, it is necessary to determine the effective anisotropic response of the REV shown in Fig. 2. This can be achieved by applying the three oscillatory relaxation experiments shown Fig. 3 (Rubino et al., 2016). Rubino et al. (2016) showed that for 2D heterogeneous samples, under plane strain conditions, it is possible to compute an equivalent homogeneous anisotropic viscoelastic solid from the strain-stress response to three relaxation tests (Fig. 3). The first test consists of the application of homogeneous time-harmonic normal displacements along the top boundary of the sample, while the lateral and bottom boundaries are confined (Fig. 3a). The second test is similar to the previous one, but the normal displacements are applied on one lateral boundary of the sample (Fig. 3b). Finally, in the third test, we apply a simple shear to the probed sample (Fig. 3c). Following Rubino et al. (2016), the average stress and strain components computed from the oscillatory relaxation tests can be related through a complex-valued and frequency-dependent equivalent stiffness matrix

$$\begin{bmatrix} <\sigma_{xx}(\omega)> \\ <\sigma_{yy}(\omega)> \\ <\sigma_{xy}(\omega)> \end{bmatrix} = \begin{bmatrix} C_{11}(\omega) & C_{12}(\omega) & C_{16}(\omega) \\ C_{12}(\omega) & C_{22}(\omega) & C_{26}(\omega) \\ C_{16}(\omega) & C_{26}(\omega) & C_{66}(\omega) \end{bmatrix} \cdot \begin{bmatrix} <\varepsilon_{xx}(\omega)> \\ <\varepsilon_{yy}(\omega)> \\ <2\varepsilon_{xy}(\omega)> \end{bmatrix}, \tag{2}$$

where the components of the equivalent stiffness matrix are evaluated for each angular frequency ω following a classic least-square fitting procedure as we have nine equations (Eq. 2 holds for the three relaxation tests) and six unknown stiffness coefficients. The angular brackets correspond to averages over the sample's volume. Once the coefficients $C_{ij}(\omega)$ are determined, it is possible to compute the equivalent seismic attenuation of P- and S-waves as a function of incidence angle and frequency following a standard procedure for anisotropic viscoelastic solids.

Finally, the spatial distribution inside the REV of a given field as a result of an arbitrarily imposed strain state can be computed as proposed by Rubino et al. (2016)

$$f_\varepsilon(x,y,\omega) = \varepsilon_{xx}(\omega) f_{11}(x,y,\omega) + \varepsilon_{yy}(\omega) f_{22}(x,y,\omega) + \varepsilon_{xy}(\omega) f_{12}(x,y,\omega), \tag{3}$$

where the strain state imposed to the sample is defined by the components ε_{xx}, ε_{yy}, and ε_{xy}. f_{11}, f_{22}, and f_{12} correspond to the desired field spatial distribution in response to strain states that have $<\varepsilon_{xx}>= 1$, $<\varepsilon_{yy}>= 1$, or $<\varepsilon_{xy}>= 1$, respectively, while the rest of the strain components are zero. It is straightforward to obtain those fields using the responses to the relaxation tests shown in Fig. 3 (Eqs. 34 to 39 in Rubino et al. (2016)). For this work, we use Eq. 3 to compute the viscous shear stress components (Eq. 1) in response to the strain state associated with body waves (i. e., P- and S-waves) propagating at varying incidence angles and frequencies.

4 Results

There are several factors potentially affecting the magnitude of wave-induced viscous shear stresses in the fluid saturating a fracture. The methodology outlined in section 3 allows to perform a sensitivity analysis of the viscous shear stress in terms of the physical properties of the viscous fluid saturating the fractures, the elastic moduli of the host rock, and the geometrical properties of the fracture network. We present our numerical results as function of the seismic wave mode (P- or S-waves), frequency, and direction of propagation. We first consider the REV shown in Fig. 2 where the side length is equal to 0.4 m and the length of both fractures is 0.36 m. The fracture aperture is 0.1 mm, which is considered within the range of realistic fracture apertures (Bakulin et al., 2000). We compare the viscous shear stresses for four cases defined by the properties given in Table 2. In addition to the reference scenario, representative of a hard rock with brine saturating the fractures, we investigate three further scenarios where we modify one property at the time. These are fluid viscosity (case 2: water instead of brine saturating the fractures), fracture aperture (case 3: wider fractures), and elastic moduli of the background medium (case 4: softer background medium).

Table 2. Physical properties utilized for the analysis of the angle and frequency dependence of τ_{xy}.

	Reference case	**Modified property**
Fluid Viscosity (η)	0.003 [Pa·s]	0.001 [Pa·s] (Case 2)
Fluid bulk modulus (K_f)	2.4 [GPa]	2.25 [GPa] (Case 2)
Fracture Aperture (h)	0.1 [mm]	0.2 [mm] (Case 3)
Background bulk modulus (K_b)	36.4 [GPa]	9 [GPa] (Case 4)
Background shear modulus (μ_b)	44 [GPa]	7 [GPa] (Case 4)

The angle dependence of τ_{xy} for both P- and S-wave incidences is obtained by first subjecting the REV to the three tests shown in Fig. 3 and then following the procedure described in Section 3. In order to compare τ_{xy} for different directions of wave propagation, we need to arbitrarily define the imposed average strain on the sample for different incidence angles. We assume that the strain associated with a seismic wave is the same for all incidence angles and equal to a realistic value. The strain amplitudes are chosen based on the magnitude of the viscous shear stress that has been found to be sufficient to initiate fracture unclogging (Manga et al., 2012). Thus, for P-waves, we used a fixed extensional strain in the direction of wave propagation such that, for the reference scenario, at 10 Hz the mean wave-induced τ_{xy} is $\sim$0.1 Pa ($\varepsilon_{\gamma\gamma} \sim 1.5{\times}10^{-7}$, where the γ-axis coincides with the direction of wave propagation). Similarly, for the analysis of S-waves, we assume that the shear strain is the same regardless of the incidence angles and equal to the value used for P-waves.

We solve the oscillatory relaxation test in the frequency-space domain (Appendix A). However, the viscous shear stress inside the REV as a function of time for a given frequency of oscillation can be written as $|\tau_{xy}(x,y,\omega)|\cos(\omega t + \phi(x,y,\omega))$, where $|\cdot|$ and ϕ represent the absolute value and the phase of a complex number, respectively. In Fig. 4, we illustrate the time evolution of the viscous shear stress in response to a 10 Hz normally incident P-wave, by computing $\tau_{ij}(x,y,t)$ at three different times: $t = 0$ s (a), $t = T/4$ (b), and $t = T/2$ (c), with T being the wave period. In order to show the details of $\tau_{xy}(x,y,t)$ inside the fracture, in Fig. 4 we only show the region delimited by the red dashed square of Fig. 2. Note that the maximum value of $\tau_{xy}(x,y,t)$ does not coincide with the time of maximal compression (Fig. 4a). Instead, it occurs approximately at a quarter of the wave period (Fig. 4b). In the following, we present results in terms of $|\tau_{xy}(\omega)|$, which corresponds to the maximum of τ_{xy} at a given position and at each frequency ω (Fig. 4d). In particular, we analyze the mean value of $|\tau_{xy}(\omega)|$ at the boundary between the fractures and the background, where unclogging is expected to take place. For brevity, we refer to this quantity as τ_{xy}.

4.1 P-wave analysis

Fig. 5a to d shows τ_{xy} as a function of incidence angle (0° to 90°) and frequency (10^0 Hz to 10^4 Hz) in response to a strain state produced by a plane P-wave. The white zones in Fig. 5a to d correspond to viscous shear stress below 0.1 Pa, which is the threshold value of fracture unclogging initiation adopted for this work. We observe that τ_{xy} increases with frequency for all incidence angles. On the basis of Eq. 1, this is expected because the fluid pressure gradient between the fractures and, hence, fluid velocity increases with frequency. Despite the different magnitudes of τ_{xy} for the different scenarios, the frequency dependence remains approximately the same for all cases. This fre-

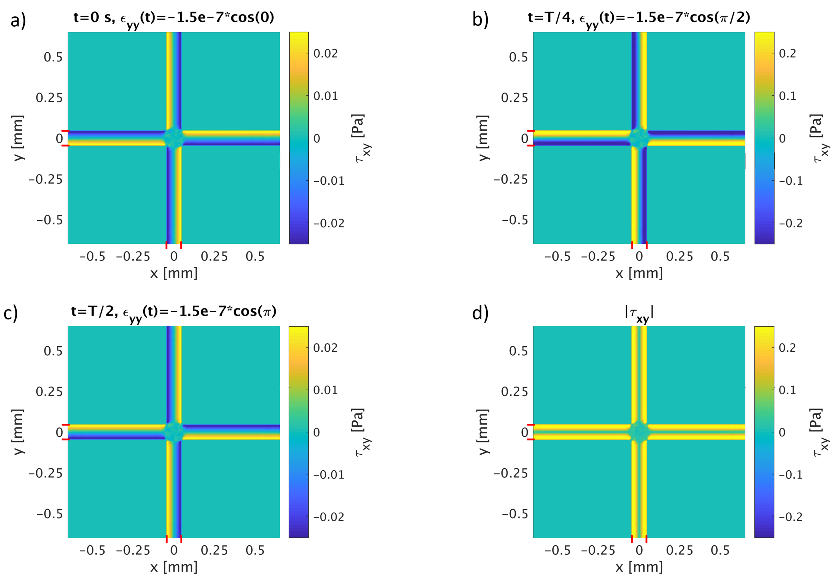

Figure 4. Time dependence of τ_{xy} in response to a normally incident P-wave having a frequency f=10 Hz. This figure shows a close-up of the dotted square shown in Fig. 2. Red marks indicate the fracture surfaces. Panels a), b), and c) correspond to times equal to 0 s (maximal compression), T/4, and T/2, respectively, where T=1/f is the wave period (note the different color ranges). Panel d) shows the absolute value of τ_{xy}, which corresponds to the maximum of the viscous shear stress developed at a given position.

quency dependence is in qualitative agreement with laboratory results (Candela et al., 2015) that point out how fracture unclogging is proportional to the increase of frequency. Fig. 5 also shows that the development (or lack) of viscous shear stresses is strongly dependent on the direction (θ) of the imposed seismic strain. For θ=0° (or θ=90°) the fluid pressure of the horizontal (vertical) fracture is much larger than that of the connected and less compressed vertical (horizontal) fracture. The corresponding pressure gradient between the fractures produces the fluid motion that we observe in the form of strong τ_{xy}. For θ=45°, and due to the fracture distribution considered, both fractures are equally compressed by the P-wave and hence experience a similar fluid pressure increase. The lack of significant fluid pressure difference between horizontal and vertical fractures implies that there is no significant fluid pressure exchange and τ_{xy} becomes negligible (Fig. 5). Interestingly, azimuthal dependence of permeability changes have been recently reported (Shi et al., 2019; Weaver et al., 2019). Shi et al. (2019) attributed the angle dependence to preferential seismically-induced unclogging for fractures with a certain orientation with respect to the direction of wave propagation.

To better understand the behavior of τ_{xy} shown in Fig. 5a to d and its relation with the FPD process between the fractures, in Fig. 5e to h we show the P-wave attenuation (Q_P^{-1}) as a function of frequency and incidence angle. The frequency dependence of Q_P^{-1} shows the typical behavior associated with the effects of FPD between connected fractures (Rubino et al., 2013). The frequency range where the fluid pressure exchange between connected fractures during a half-cycle of the wave is maximum, leading to maximal seismic attenuation, is directly proportional to an effective diffusivity of the fractured medium and inversely proportional to the distance between the tip of a fracture and its connection with another one (Rubino et al., 2014; Guo et al., 2017). The former corresponds to the diffusivity of an effective porous medium where fractures parallel to

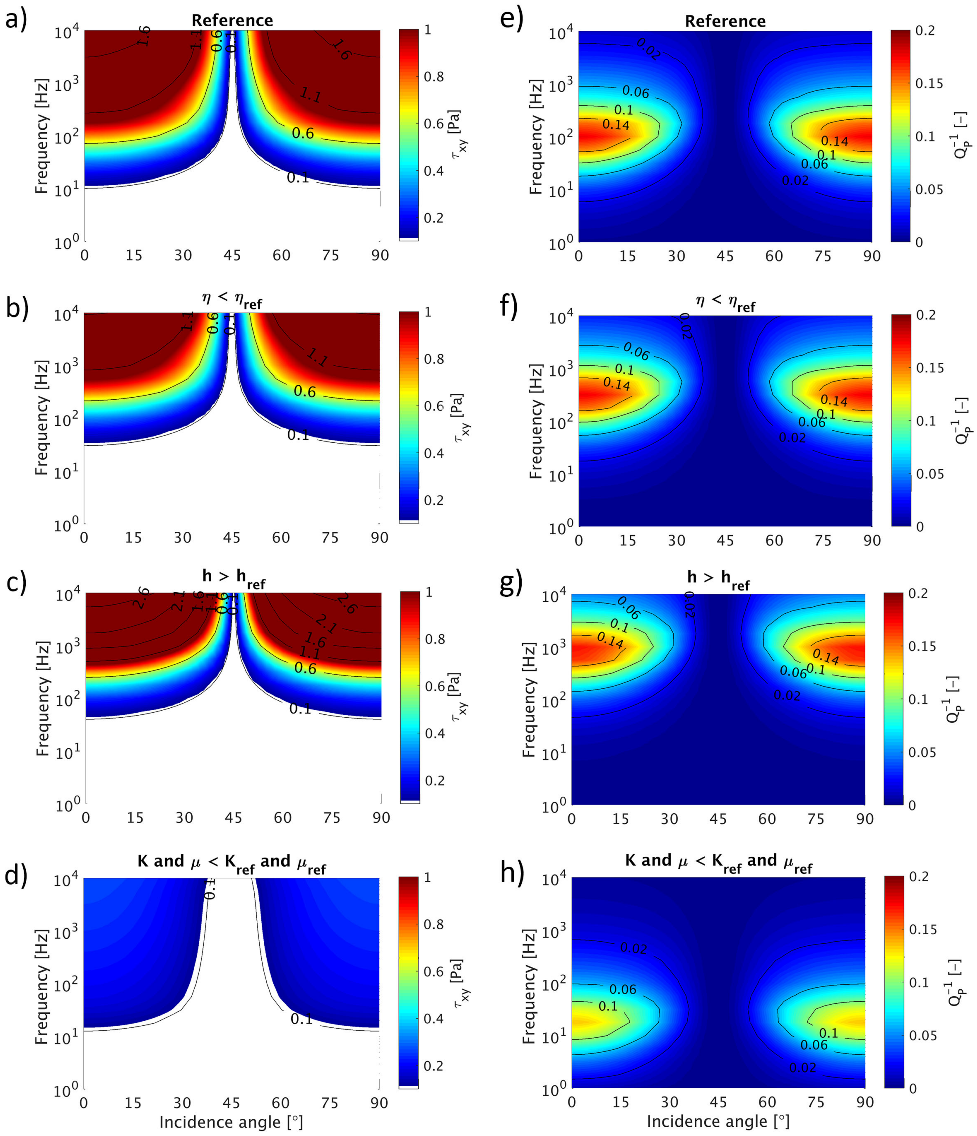

Figure 5. P-wave-induced viscous shear stress at fracture interfaces (left column) and P-wave attenuation (right column) as functions of frequency and incidence angle. The REV properties used for the sensitivity analysis are described in Table 2. White zones in panels a) to d) indicate values of τ_{xy} below the viscous shear stress threshold of 0.1 Pa. Reducing the fluid viscosity (panel b) shifts the threshold to higher frequencies. Increasing the fracture aperture (panel c) shifts the threshold to higher frequencies. Reducing the background bulk shear moduli (panel d) shifts the threshold to lower frequencies. Note the correlation between the changes in the attenuation peak frequency for different physical properties in panels e) to h) and the frequency shifts of the viscous shear stress threshold in panels a) to d).

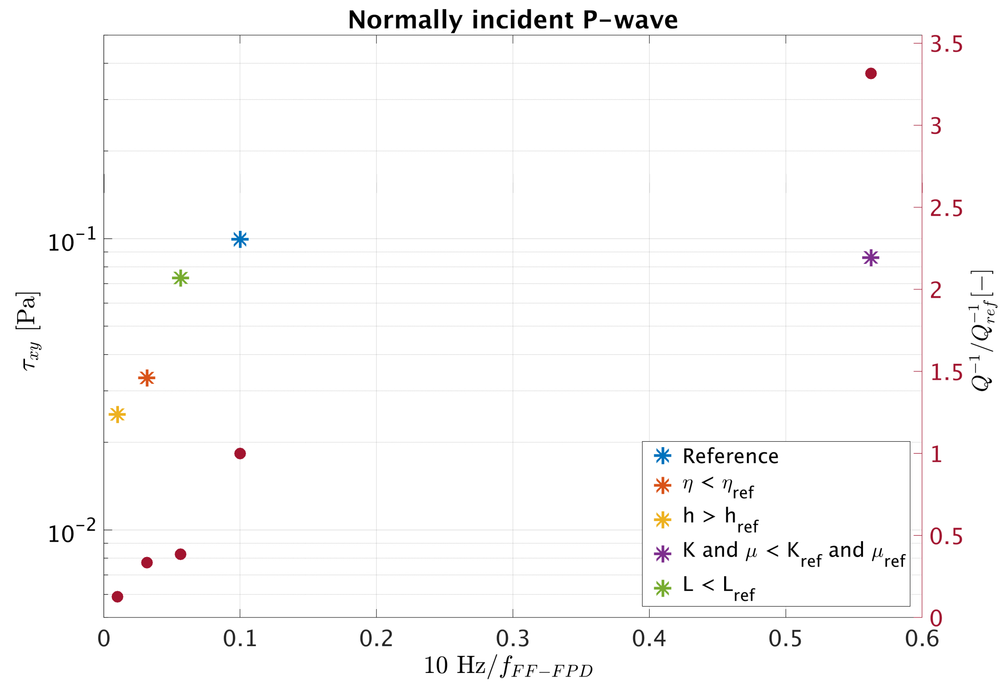

Figure 6. Viscous shear stress along the interface fluid-fracture wall as function of a normalized frequency for a normally incident P-wave (stars). Red dots correspond to the ratio between the attenuation for each case and the attenuation of the reference scenario at 10 Hz. The REV properties for each case are described in Table 2. The case L<L_{ref} corresponds to a fracture length of 0.28 m instead of 0.36 m.

the direction of the wave propagation front and the background act as the pore space and the solid phase, respectively. Note that the frequency shifts of the viscous shear stress threshold for different physical properties (Fig. 5a to d) follow the changes of the attenuation peak frequency in Fig. 5e to h. Lower fluid viscosity (Fig. 5f) as well as larger fracture aperture (Fig. 5g) shift the attenuation peak frequency (f_{FF-FPD}) towards higher frequencies. As a consequence, lower values of τ_{xy} compared to the reference scenario are observed at low frequencies (compare Fig. 5a with Figs. 5b and c). An interesting effect occurs for lower background elastic moduli as it shifts f_{FF-FPD} towards lower frequencies (Fig. 5h). However, this is not manifested as a higher τ_{xy} at low frequencies compared with the reference scenario. This is due to the fact that a reduced compressibility contrast produces a reduced pressure gradient between the connected fractures and, hence, less pronounced FF-FPD effects. Nevertheless, the levels of τ_{xy} are still above 0.1 Pa (Fig. 5d).

The analysis of Fig. 5 shows that spatially varying properties may lead to different levels of τ_{xy} and correspondingly of fracture unclogging. We can further quantify the changes in the magnitude of τ_{xy} with varying physical properties by plotting τ_{xy} as a function of the ratio between the seismic wave frequency (10 Hz) and f_{FF-FPD} for each case (Fig. 6). In general, as the seismic wave frequency approaches f_{FF-FPD}, τ_{xy} is expected to increase. A fluid viscosity decrease from 0.003 Pa.s to 0.001 Pa.s produces a decrease in τ_{xy} of ∼70% for a fixed seismic frequency. Even larger changes in τ_{xy} occur when the aperture of the fractures is doubled with respect to the reference scenario. We also include in Fig. 6 the ratio between the attenuation of each case and the attenuation of the reference scenario at 10 Hz. Fig. 6 shows that the changes in attenuation with respect to the reference scenario follow a similar trend as τ_{xy}. Fig. 6 also compares the responses when the fracture length is changed from 0.36 m to 0.28 m (case L<L$_{ref}$). This is an interesting case regarding the link between τ_{xy} and the changes in seismic attenuation. We note that by decreasing the aspect ratio of the fractures, the attenuation does not increase as much as expected from the comparison with the other cases. This is due to the smaller fluid storage volume involved in the FPD process. On the other hand, the seismically-induced τ_{xy} is slightly larger than expected. For a background medium characterised by lower bulk and shear moduli compared with the reference scenario, the decrease in f_{FF-FPD} results in a higher seismic attenuation. However, this does not translate into higher levels of τ_{xy} as pointed out in Fig. 5d. Although the relative changes in seismic attenuation are not always straightforwardly associated with the variations of τ_{xy}, they can provide valuable insight on the regions that are more affected by fracture unclogging in a reservoir.

4.2 S-wave analysis and comparison with P-waves

The frequency and angle dependence of τ_{xy} as a result of the strain state produced by a plane S-wave is shown in Fig. 7a to d. As for P-waves, we observe that for a given fixed seismic strain imposed to the sample, τ_{xy} increases with frequency. S-waves show maximal τ_{xy} for θ=45° (Fig. 7). As pointed out by Rubino et al. (2017), the induced pressures have opposite signs in the horizontal and vertical fractures, respectively, which results in a particularly large pressure gradient between them. This, in turn, is observed in Fig. 7 as a large τ_{xy} at θ=45°. At horizontal and normal incident directions of S-wave propagation, the fluid pressure increase inside the fractures is negligible and, correspondingly, τ_{xy} approaches zero. As for P-waves, the behavior of τ_{xy} observed in Fig. 7a to d follows a similar angle dependence as the S-wave attenuation (Fig. 7e to h) due to the link between the development of strong viscous shear stresses and the fluid pressure diffusion process that produces the seismic energy dissipation. For completeness, in Fig. 8, we quantify the changes in τ_{xy} for the different cases of Table 2 as well as for the case L<L$_{ref}$.

Comparison of the effects imposed by P- and S-waves (Fig. 6 and 8) suggests that S-waves produce larger transient τ_{xy} for equal extensional and shear strain, respectively. Fig. 9 expands on the dependence of τ_{xy} with the magnitude of the seismic strain for P- and S-waves. We consider a frequency-dependent $\varepsilon_{\gamma\gamma}$ such that, at each frequency, τ_{xy}=0.1 Pa at normal P-wave incidence. The frequencies considered are 1, 10 and 100 Hz. We observe that in order to obtain the same magnitude of τ_{xy}, a decrease in one order of magnitude in seismic wave frequency, requires an increase of approximately one order of magnitude in the seismic strain. Lastly, Fig. 9b shows that for the same values of seismic strain, S-waves propagating at 45° produce τ_{xy} approximately two times larger than P-waves at normal incidence. Note that a rotation of the orthogonal system of fractures with respect to the vertical axis would produce a similar rotation in the angle dependence shown in Fig. 9.

4.3 Stochastic fracture networks

The analysis shown in Section 4 assumes an REV having two orthogonal intersecting fractures (Fig. 2). Such scenario is useful to illustrate the development of seismically-induced viscous shear stress for different physical properties in anisotropic fractured rocks. In this section, we analyze with more detail the impact on τ_{xy} of fracture network properties such as the fracture length distribution, the fracture density, and the degree of fracture connectivity. To do so, we generate stochastic fracture networks in a sample as in Hunziker et al. (2018) assuming that the number of fractures as function of their length

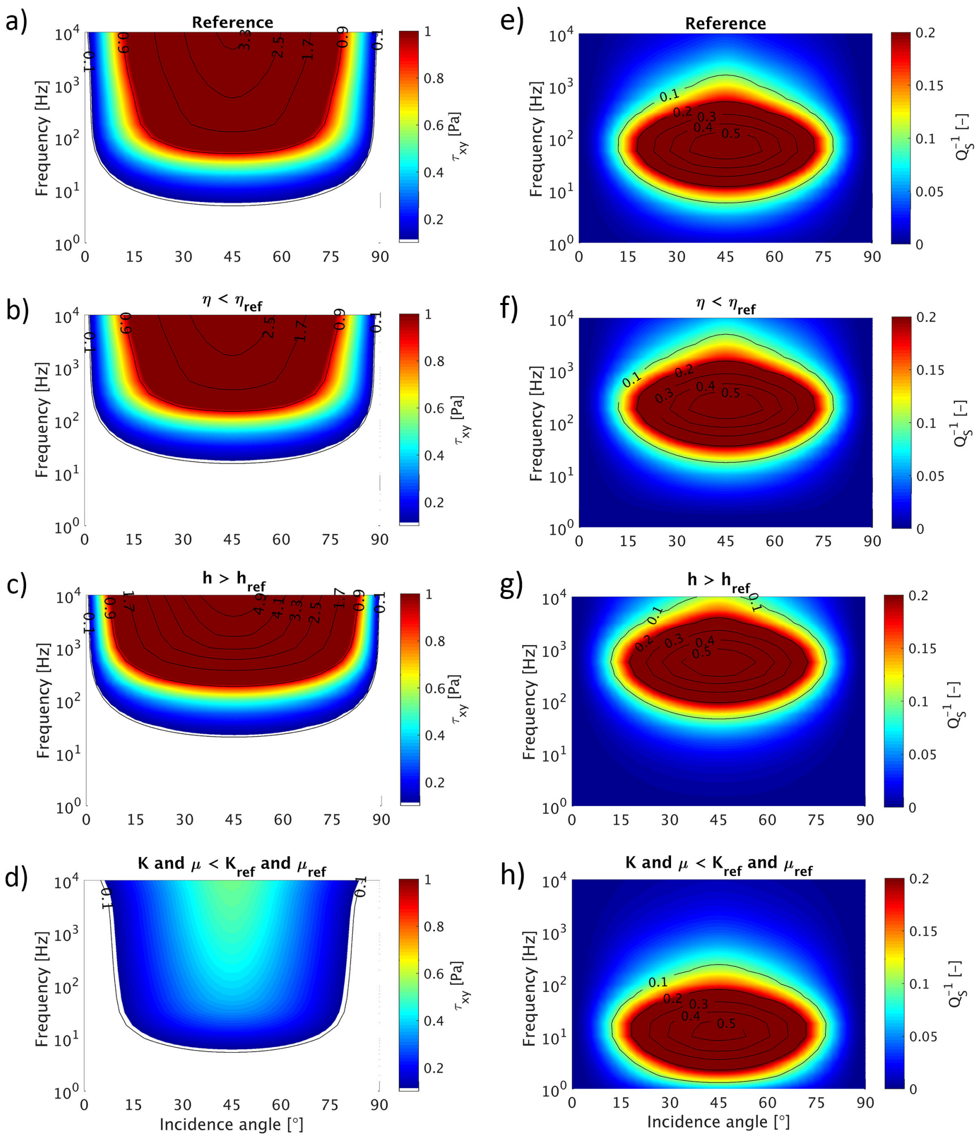

Figure 7. S-wave-induced viscous shear stress at the fracture interfaces (left column) and S-wave attenuation (right column) as functions of frequency and incidence angle. The REV properties used for the sensitivity analysis are described in Table 2. White zones in panels a) to d) indicate values of τ_{xy} below the viscous shear stress threshold of 0.1 Pa. The threshold frequency follows a similar trend as for P-waves (Fig. 5).

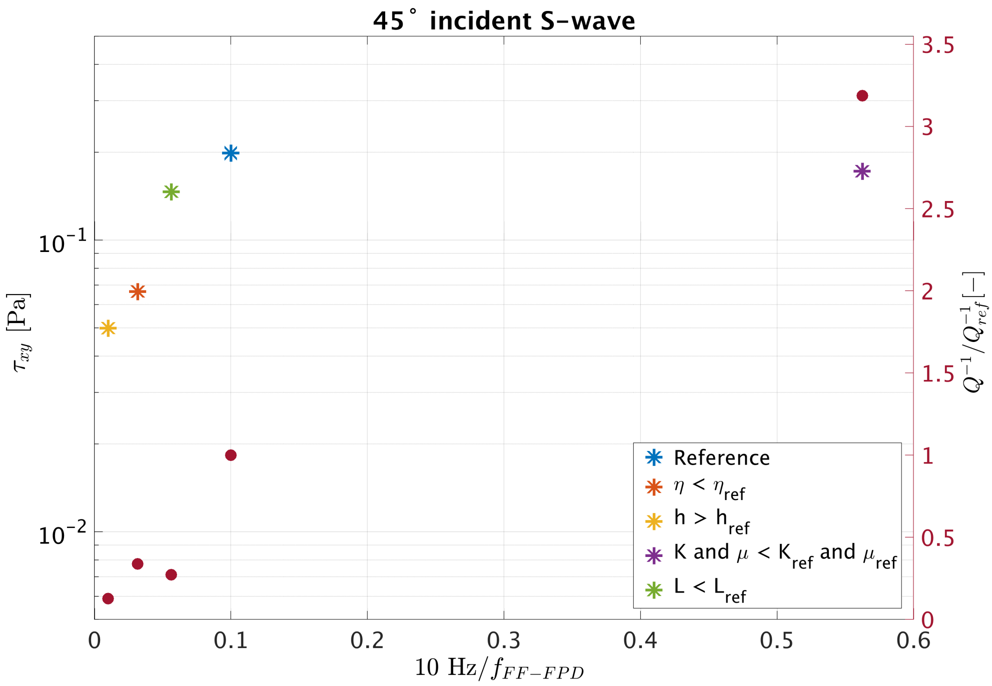

Figure 8. Viscous shear stress along the interface fluid-fracture wall as function of a normalized frequency for a 45° incident S-wave (stars). Red dots correspond to the ratio between the attenuation for each case and the attenuation of the reference scenario at 10 Hz. The REV properties for each case are described in Table 2. The case L<L_{ref} corresponds to a fracture length of 0.28 m instead of 0.36 m.

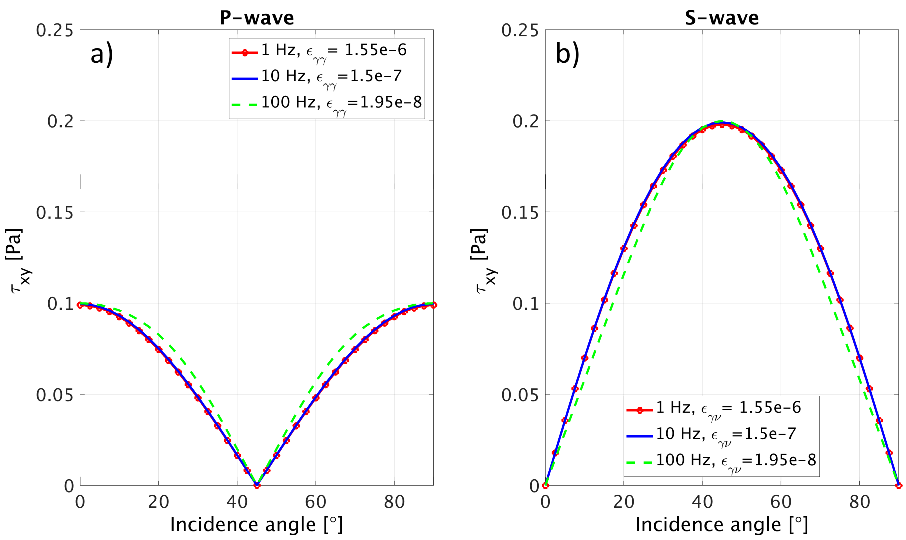

Figure 9. Wave-induced τ_{xy} as a function of the incidence angle. Panels a) and b) show P- and S-waves, respectively. The physical properties correspond to those of the reference case in Table 2. For equal seismic strain values, the maximal τ_{xy} produced by S-waves is larger than the maximal τ_{xy} associated with P-waves.

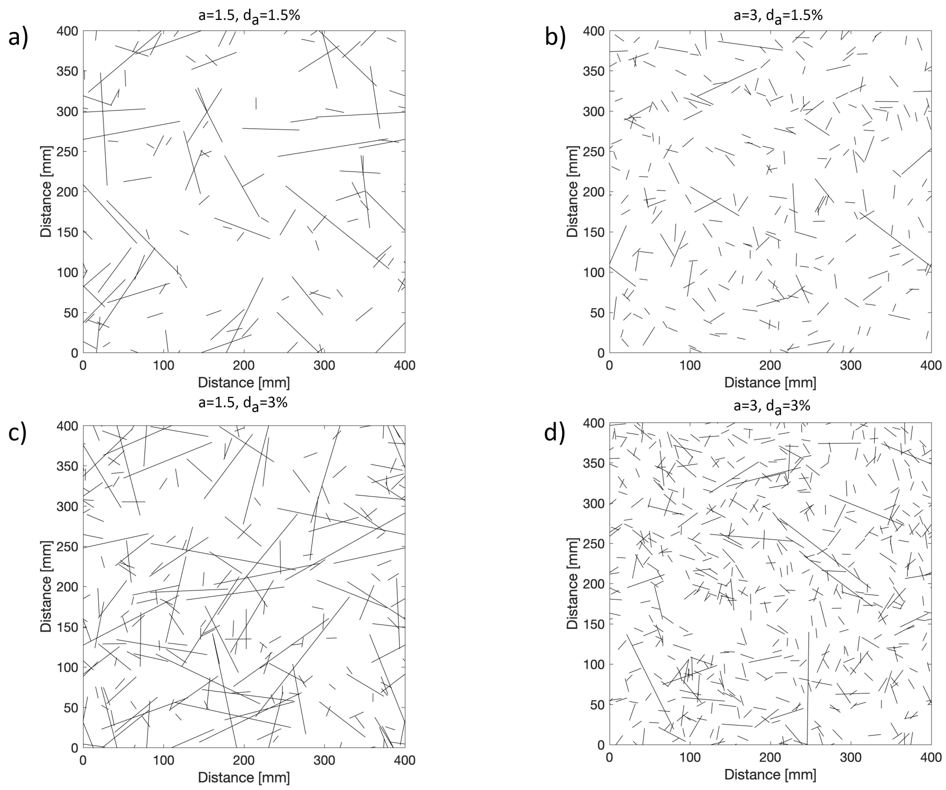

Figure 10. Synthetic samples representative of four 2D fractured media. The samples have different stochastic fracture networks with length distributions generated using Eq. 4. A larger value of a produces more shorter fractures (b and d), while a smaller value of a produces an increasing probability of larger fractures (a and c). d_a denotes the fracture density which varies between 1.5% (a and b) and 3% (c and d).

l can be described as (de Dreuzy et al., 2001)

$$n(l) = d_a(a-1)\frac{l^{-a}}{l_{min}^{-a+1}}, \tag{4}$$

where $l \in [l_{min}, l_{max}]$ with the maximum fracture length l_{max} being half of the side length of the REV, and the minimum length of the fractures l_{min} set to 1 cm. An interesting feature of Eq. 4 is that it allows to control the number of fractures of a given length $n(l)$ with two parameters. The exponent a controls the relative probability of longer and shorter fractures. The second parameter is the fracture density d_a, which is the area covered by fractures per unit area. In order to minimize the effects due to an anisotropic fracture distribution, the orientations of the fractures and the positions of the fracture centers are drawn from a uniform distribution as in Hunziker et al. (2018). As a consequence, the fractured medium is effectively isotropic. For the analysis, the thickness of all fractures is constant and equal to 0.5 mm. Fig. 10 illustrates the diversity of the considered stochastic fracture networks. We consider two fracture densities d_a (1.5% and 3%) and two characteristic exponents of the fracture size distribution a (1.5 and 3). Increasing the parameter a increases the number of shorter fractures with respect to the longer ones (e.g., Figs. 10a and b) while increasing the fracture density d_a increases the number of fractures in the sample (e.g., Figs. 10a and c).

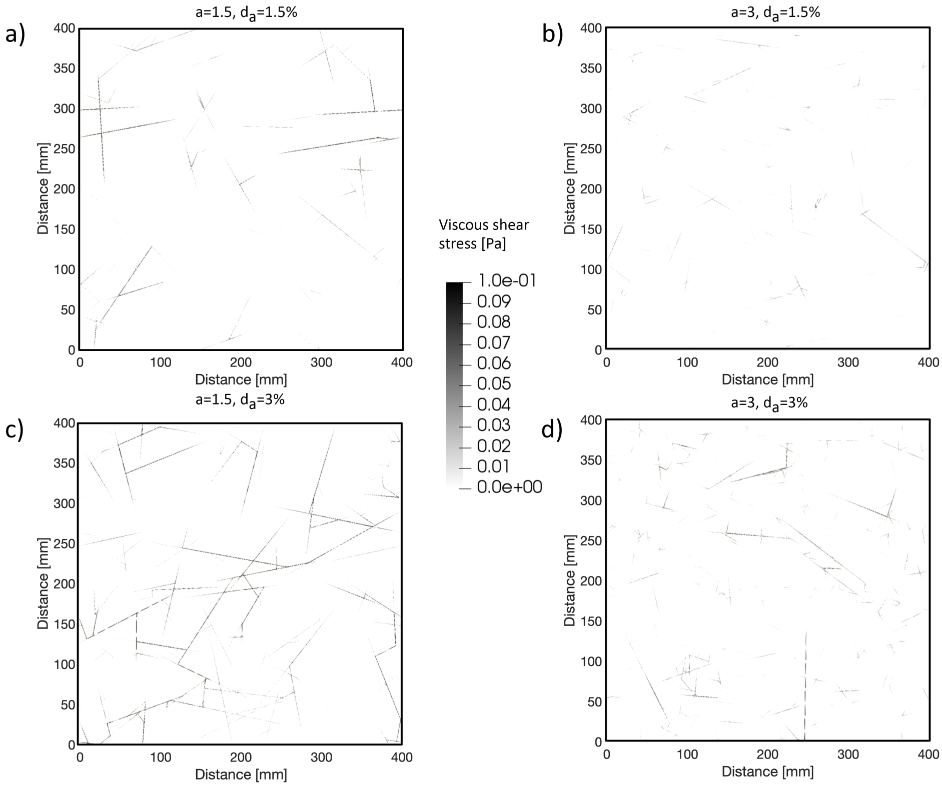

Figure 11. Distribution of τ_{xy} inside the fractures of the samples shown in Fig. 10. The observed τ_{xy} distribution results from the strain associated with a propagating P-wave with a frequency f=10 Hz. For a fixed fracture density, higher levels of τ_{xy} are observed for fracture networks with larger number of long fractures due to the increased fracture characteristic length and connectivity (e.g., comparison of panels c and d).

In Fig. 11, we plot the viscous shear stress distribution for the different fracture networks shown in Fig. 10. The strain state corresponds to a normally incident P-wave of f=10 Hz with $\varepsilon_{zz} = 3 \times 10^{-5}$, which is obtained by subjecting the different samples to the vertical relaxation test illustrated in Fig. 3a. We limit the analysis to normal incidence due to the isotropic seismic response of the sample. Fig. 11 shows that samples with larger fracture density as well as a lower parameter a exhibit higher values of τ_{xy} in the samples. The increase for higher fracture density is expected as it increases the fluid storage volume contributing to the FPD process for a fixed sample size. The correlation between τ_{xy} and the parameter a is related to the characteristic fracture length involved in the FPD process and the degree of fracture connectivity in the sample. A decreasing value of a results in a lower number of shorter fractures and thus in an increase of the characteristic time scale of the FPD process, which in turn leads to a shift of f_{FF-FPD} towards the low frequency range (Hunziker et al., 2018). From the analysis of Fig. 6, the corresponding larger ratio between the considered frequency and f_{FF-FPD} is expected to be reflected in higher levels of τ_{xy}. At the same time, a decreasing value of a increases the number of fracture connections due to the presence of longer fractures. This in turn increases the amount of fluid storage volume contributing to the FPD.

In Fig. 12, we quantify this analysis by computing the viscous shear stress per unit of fracture area in the sample. We normalize by the area occupied by the fractures (A_{frac})

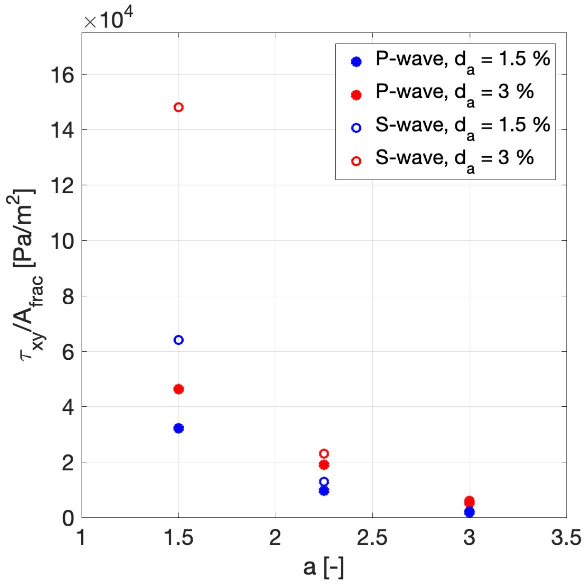

Figure 12. τ_{xy} **per unit of fracture area (**A_{frac}**) as a function of the parameter** a **of Eq. 4.** Filled and empty circles correspond to P- and S-waves, respectively. Blue and red colors represent fracture densities of 1.5 and 3%. The quantity τ_{xy}/A_{frac} decreases exponentially with a (i.e., as the number of short unconnected fractures increases).

in the sample to compare cases with different fracture density. We consider the same cases shown in Fig. 10 plus an intermediate case given by a=2.25. It is important to mention that the values plotted in Fig. 12 represent a single realization for each case. For completeness, we also plot the values for S-waves. We observe that as the number of longer fractures, and, hence, the characteristic length and degree of connectivity, in the sample increases (decreasing a), the quantity τ_{xy}/A_{frac} increases exponentially. Lastly, although P- and S-waves produce comparable levels of τ_{xy}/A_{frac}, S-waves are more efficient than P-waves to produce large viscous shear stress.

4.4 Effect of fracture geometry

Until now, we have computed τ_{xy} utilizing 2D samples (Figs. 2 and 10). A disadvantage of considering 2D samples is that we cannot properly model the effects associated with a spatially heterogeneous fracture aperture. The reason is that 2D simulations assume that fractures extend infinitely in the third dimension and, hence, local variations in fracture aperture cannot be modelled. In the following, we study the effects of fracture aperture distribution by considering the 3D sample shown in Fig. 13. For brevity we only subject the sample to one oscillatory relaxation test in which a normal displacement is applied along the top surface of the sample, while the lateral and bottom surfaces are confined. This is a 3D generalization of the 2D test shown in Fig. 3a, and is representative of the action of a normally incident P-wave. The fracture aperture distribution is characterized by regions of zero aperture (contact areas) and regions with aperture h=1 mm (open areas). Contact and open regions are represented with background and fluid properties, respectively. The corresponding fluid and elastic background physical properties are those given in Table 2 for the reference scenario. The aperture distribution of the vertical and horizontal fractures in the REV of Fig. 13 is assumed to be the same. Following Pyrak-Nolte and Nolte (2016), the aperture distribution of the fractures was generated using the stratified percolation approach of Nolte and Pyrak-

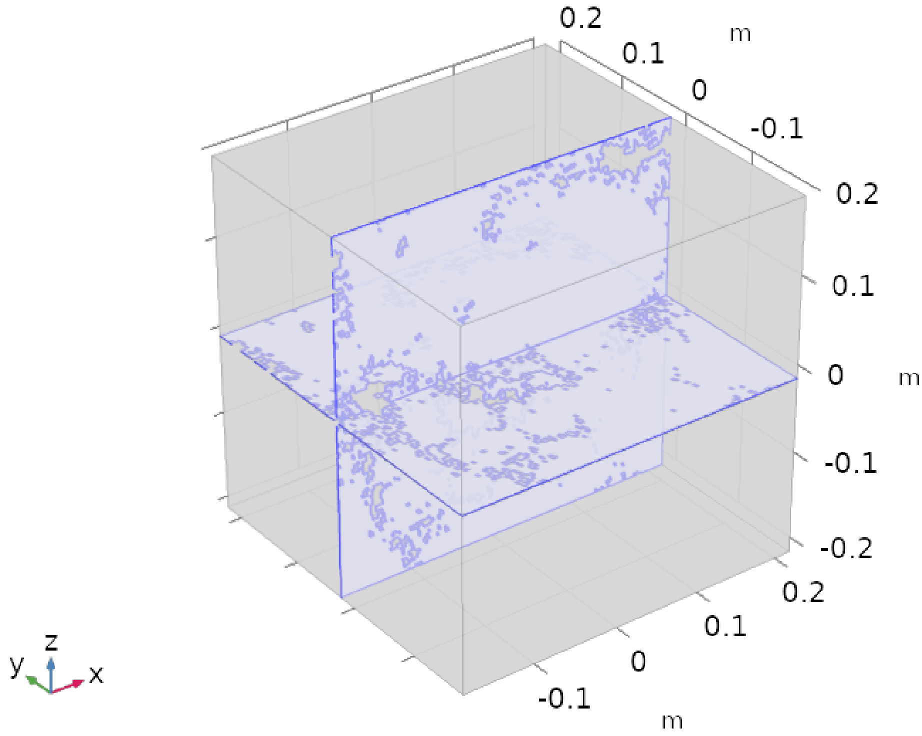

Figure 13. Synthetic sample representing a unit cell of a 3D periodically fractured rock. The sample contains two connected orthogonal fluid-saturated fractures. 3D samples allow for modelling contact areas between the fracture walls which is not possible for 2D samples as they would extend infinitely in the third dimension thus affecting the effective length of the fractures.

Nolte (1991). A detailed explanation of the fracture aperture distribution generation, which is based on a recursive algorithm that defines a self-similar cascade can be found in Lissa et al. (2019). One of the most important advantages of this model is that it allows to control the characteristic correlation length of the contact areas. Due to the higher computational cost of the 3D simulations and to avoid problems with the meshing process, we have considered an open fracture aperture 10 and 2 times larger than for the 2D samples shown in Figs. 2 and 10, respectively. Given that a thicker fracture increases f_{FF-FPD} (e.g., Fig.6), we impose a seismic strain of $\varepsilon_{zz} = 2 \times 10^{-5}$ to have viscous shear stress values above 0.1 Pa for all the analyzed cases.

We first consider the case of two fracture aperture distributions with correlated (long characteristic length) and uncorrelated (short characteristic length) contact area distributions (Fig. 14a and c, respectively). Both fractures have contact area density equal to 10%, which means that the volume fraction of fractures is the same for both models. Note that in Fig. 14 we only plot the aperture distribution for the vertical fracture as it is the same for the horizontal one. For brevity, in Figs. 14b and d we only show the component of the viscous shear stress tensor τ_{yz} because it is the most affected by FPD between fractures due to the spatial distribution of the fractures. We only plot τ_{yz} for the vertical fracture because it shows a similar behavior in the horizontal fracture. Cold and hot colours in Fig. 14 denote low and high τ_{yz}, respectively, while contact areas are plotted in black. Despite the spatially heterogeneous distribution of τ_{yz} associated with the geometry of the contact areas, large values of τ_{yz} are still present in the open fracture regions. Due to the spatial distribution of the contact areas, the correlated fracture is mechanically more compliant than the uncorrelated one. This results in larger τ_{yz} in the case of the fracture with correlated contact area distribution (Fig. 14b) compared with an uncorrelated distribution. Moreover, although τ_{yz} tends to increase in the vicinity of contact areas, the channelized flows produced by the contact area distribution seems to dominate the development of large viscous shearing. In particular, contact area distributions can significantly affect the hydraulic connectivity between the intersecting fractures. This, in turn, drastically changes the levels of τ_{yz} (note the different color scales in Figs. 14b and d).

In order to minimize the effect of the compressibility contrast between the fractures and the background, we consider the contact area distribution shown in Fig. 14e, which results in a similar fracture compliance as the one shown in Fig. 14a ($\sim$ 2.5% relative difference). To produce similar mechanical compliance for correlated and uncorrelated distributions, the contact area density has been decreased from 10% to 2.6%. Fig. 14f shows that, as a consequence of the uncorrelated contact area distribution, τ_{yz} exhibits a channelized pattern as in Fig. 14d. However, the levels of τ_{yz} are larger than in Fig. 14d due to the higher compressibility contrast between the fractures and the background (note the different color scales in Fig. 14d and f).

5 Discussion

5.1 Permeability changes due to fracture unclogging

The question regarding how seismically-induced viscous shearing changes the permeability of a reservoir due to fracture unclogging remains unexplored in this work (Fig. 1 arrow c). Our study is limited to the analysis of the development of strong viscous shear stress in the fluid saturating a fracture. Following previous studies, we adopted a threshold value of τ_{xy}=0.1 Pa to indicate potential fracture unclogging initiation. The representativeness of this value for the physical properties of the rock as well as for the characteristics of the seismic waves analyzed in this work is speculative. Nevertheless, we can qualitatively verify the validity of the adopted threshold. Elkhoury et al. (2006) found that the permeability changes ($\Delta\kappa$) in a reservoir follow a linear trend with the dynamic shear strain imposed by the waves of earthquakes. This observation is in qualitative agree-

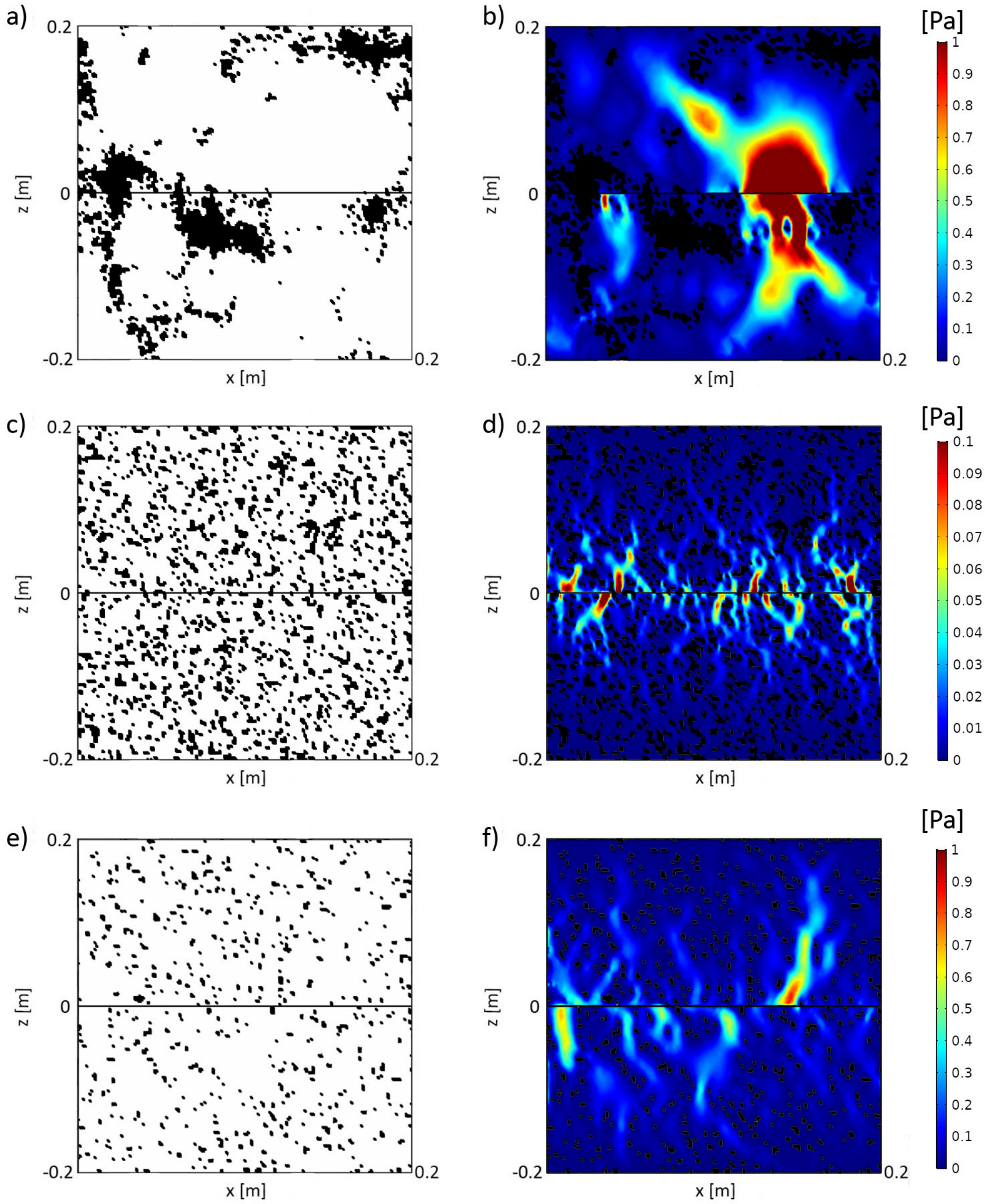

Figure 14. Fracture geometry (left column) and $|\tau_{yz}|$ for f=10 Hz and P-wave incidence (right column). The plots are computed at one of the interfaces between each fracture and the background. Black and white regions in a, c, and e illustrate contact areas and open fracture, respectively. Panels a and c correspond to fractures with same volume but correlated and uncorrelated contact area distributions, respectively. Panels a and e correspond to fractures with same compliance under dry conditions but with different contact area correlation length. Note the different color scales in panels b, d, and f.

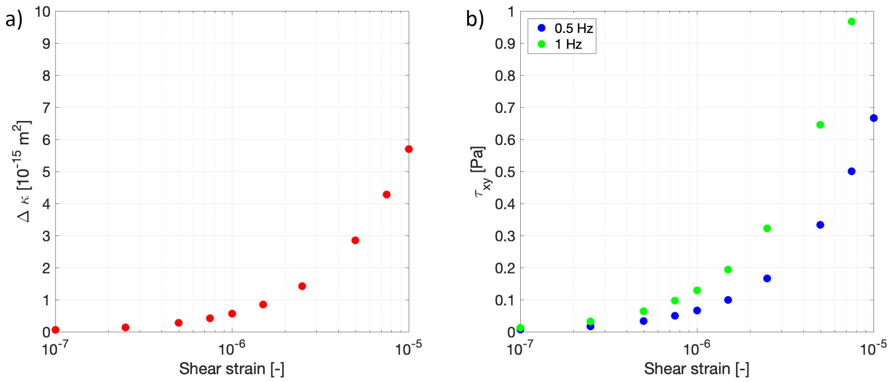

Figure 15. Validity of τ_{xy}=0.1 Pa as a threshold for fracture unclogging initiation. Panel a shows the relation between seismic shear strain and increase in reservoir permeability found by Elkhoury et al. (2006). Panel b shows the relation between seismic shear strain and viscous shear stress from our numerical simulations.

ment with laboratory experiments (Elkhoury et al., 2011; Candela et al., 2014). These have also shown that the magnitude of the permeability enhancement due to fracture unclogging scales with the amplitude of the dynamic strain for a fixed frequency.

Elkhoury et al. (2006) quantified the above mentioned linear relation using measurements from two wells. Fig. 15a shows the strain-$\Delta\kappa$ relation assuming the mean value of the two slopes obtained by Elkhoury et al. (2006). Note that we use a logarithmic x-axis to plot the linear strain-$\Delta\kappa$ relation. They observed permeability changes as small as $0.5{\times}10^{-15}$m^2, which correspond to shear strains in the order of $1{\times}10^{-6}$. On the other hand, we can plot the relation between the shear strain (for a 45° incident S-wave) and the viscous shear stress for the same properties considered in the analysis of Fig. 9. In Fig. 15b, we plot the relation for two frequencies (0.5 and 1 Hz) that are close to the frequency of the signals analyzed by Elkhoury et al. (2006). Assuming that the strain-$\Delta\kappa$ relation found by Elkhoury et al. (2006) also holds for our fractured medium, we would expect fracture unclogging effects at shear strains in the order of $1{\times}10^{-6}$. Indeed, those strain values produce viscous shear stresses that are very close to 0.1 Pa for the frequencies considered. This supports not only our theoretical modelling but also the viscous shearing threshold adopted. Lastly, note that as the seismic shear strain increases, our simulated τ_{xy} increases while the observed $\Delta\kappa$ increases as well. This agreement further supports fracture unclogging as the mechanism of permeability increase.

5.2 Fluid motion modelling

The frequencies considered in our study belong to the seismic frequency range. However, in Figs. 5 and 7, we illustrate the frequency dependence of τ_{xy} up to sonic frequencies. For relatively high frequencies, it is important to verify the validity of the assumptions of the proposed numerical upscaling. One of the assumptions is related to the modelling of the fluid motion in the fractures in which advective acceleration terms are assumed to be small compared to the viscous terms in the Navier-Stokes equations (Appendix A). The condition for the inertia forces to be negligible compared to the viscous forces requires the reduced Reynolds number $Re^\star = Re\alpha << 1$ (Zimmerman & Main, 2004). The Reynolds number Re can be approximated as $\rho_f \tau_{xy} h^2/\eta^2$ and α is the aspect ratio of the fracture. The frequency dependence of $Re^\star$ is given through $\tau_{xy}(\omega)$. For the parameters in Table 2, and the maximal τ_{xy} observed in Figs. 5 and 7, $Re^\star < 0.01$. This means that for the order of magnitude of τ_{xy} analyzed, our approach is valid. Another assumption that must be examined for all frequencies is the validity of an effective medium representation of the fractured sample. This assumption requires $\lambda \gg$ REV, where $\lambda = v/f$ is the wavelength and v the seismic wave phase velocity. At 10 kHz, the wavelengths become comparable to the size of the REV and departures from effective medium responses are expected to arise. Although for the relatively low frequency (10 Hz) considered in the sensitivity analysis performed in this work these assumptions are fulfilled, it is important to remark that the validity of both assumptions is extremely dependent on the fluid, background and fracture properties. Lastly, it is important to mention that we use the same mesh for all frequencies analyzed. In this case, the mesh needs to be fine enough to be able to capture the spatial variability of the FPD process at the highest frequency of interest. Additional information on the discretization process can be found in Figures S1 to S3 of Supporting Information.

5.3 Application of the methodology to surface waves

The numerical strategy utilized in this work, and Eq. 3 in particular, allows to quantify the spatial distribution of a desired field, such as fluid displacement or pressure, in response to arbitrary strain states of the REV. We have computed the viscous shear forces in response to the action of body waves at arbitrary directions of wave propagation. This is in line with the laboratory experiments shown in section 2, which in most cases reproduce the action of a compressional wave to study fracture unclogging. Moreover, recent studies have shown that body waves characterised by relatively high frequencies may impose strain rates in the order of 10^{-5} and affect the fluid pressure in a reservoir (Lupi et al., 2013; Lupi, Fuchs, & Saenger, 2017). However, most of the field evidence suggests that the seismic strain inducing pore fluid pressure changes in reservoirs is predominantly related to surface waves (Brodsky et al., 2003; Manga & Brodsky, 2006; C.-Y. Wang, 2007). Moreover, most of the available field observations of fracture unclogging effects rely on the analysis of surface waves (Manga et al., 2012). As an example, Taira et al. (2018) recently used an ambient noise-based seismic interferometry approach to show that the Salton Sea geothermal field experienced a number of sudden surface wave velocity reductions in response to the dynamic stresses from local and regional earthquakes. They interpret the reduction of velocity as an increase of apparent fracture density due to the unclogging of fractures in response to the seismically induced pore pressure fluctuations. We have computed the effects of body plane waves due to the simplicity of the analytical solution of the strain produced by them. Given that the strain state associated with a surface wave can be thought as a superposition of compressional and shear modes (Carcione, 2007), we believe that our analysis is also meaningful to understand the effects of surface waves. Nevertheless, extending our analysis to consider strains states typical of surface waves as the source of the pressure oscillations that create viscous shearing in the fractures will be part of our future studies.

5.4 Seismic stimulation

As a result of documented field and laboratory experiments, it has been suggested that stimulation of reservoirs with low-amplitude stresses could be a possible method for active permeability enhancement. This is particularly relevant in engineered systems where permeability is critically important, for example, in enhanced geothermal systems (Manga et al., 2012). Indeed, the use of stimulation through the application of dynamic shaking has a long history of study for enhanced oil recovery. Beresnev and Johnson (1994) reviewed a series of laboratory and field studies covering the seismic-ultrasonic frequency range that support and test the use of seismic stimulation for enhanced oil recovery. Pride et al. (2008) refer to the common practice of using downhole seismic sources in stimulation wells for oil-reservoir stimulation. In that case, seismic waves are created by a sudden release of fluid inside the borehole. Although our results suggest that dynamically changing permeability of fractured systems may be feasible, we acknowledge the engineering challenges that artificial stimulation of reservoirs represent. Karve et al. (2017) pointed out that the effectiveness of seismic stimulation for enhanced oil recovery using artificial sources, such as, for example, a fleet of surface vibrators or downhole hydraulic pumps, depends on the strength and spatial extent of the wave motion in the oil reservoir. They proposed an optimization-based algorithm for designing an efficient wave energy delivery system to generate the wave motion of the required magnitude in the reservoir. Regarding the exposure time to seismic stimulation, Kocharyan et al. (2011) found that as the imposed strain decreases, a substantially longer exposure to vibrations is required for the permeability of a crack to increase. Our work points out that future research should be focused on exploring the impact of enhanced oil recovery technologies on fracture unclogging considering additional factors, such as directivity, radiation pattern, stimulation duration, and reservoir structure, which are expected to influence the magnitude of the seismically-induced viscous shearing. The methodology used in this work to obtain the viscous shear stress inside an REV of a given formation of interest due to an arbitrary strain state can help to find the corresponding set up optimization.

5.5 Laboratory experiments

The results shown in Section 4.4 are in qualitative agreement with the findings of Kutay and Aydilek (2009), which suggested that the maximum shear stresses caused by the viscous fluid movement can be generated at pore space constrictions. In the study of Kutay and Aydilek (2009), large viscous shearing due to water flow within the pore structure of an asphalt was believed to cause the asphalt binder to separate from the aggregate surface. In the case of fractures, the viscous shearing is significantly affected by the fracture aperture distribution which, in turn, may produce spatially variable fracture unclogging. Pyrak-Nolte and Morris (2000) showed that, as a result of the contact area distribution, uncorrelated fractures tend to develop multiple flow paths making them less sensitive to aperture changes (e.g., due to increasing loading) than correlated ones. In addition to the different levels of viscous shearing developed for correlated and uncorrelated fractures, this may indicate that fracture unclogging effects are more easily observed in correlated fractures. Manga et al. (2012) speculated that the differences in the permeability response observed in some of the experiments listed in Table 1 are likely due to the fracturing mechanism, the type of applied oscillation, and the frequency of the oscillation. The effects associated with the internal structure of the fracture observed in Fig. 14 may also explain some of the differences in permeability changes observed in the laboratory. Although in our simulations the fracture properties are invariant during and after the passage of the seismic waves, the study of the evolution of the aperture of fractures as a result of the mobilization of particles can be addressed in the future.

6 Conclusions

We performed numerical simulations to assess the potential of seismic waves to produce viscous shear stresses in fluid saturated fractures that are strong enough to initiate fracture unclogging. Our results show that seismically induced viscous shearing in the order of those initiating fracture unclogging (0.1 to 1 Pa) are plausible for strain magnitudes and frequencies typically observed in field and laboratory measurements. In agreement with previously reported laboratory experiments, viscous shear stress was observed to increase with frequency and seismic strain magnitude. For a relatively simple system of orthogonal intersecting fractures, the development of viscous shear stress strongly depends on the direction of wave propagation and this anisotropy is different for P- and S-waves. P- and S-wave related effects are at its minimum and maximum, respectively, at 45° incidence angle. Moreover, for the same magnitude of seismic strain, the maximal τ_{xy} produced by S-waves was found to be approximately two times larger than the maximal effects of P-waves. This points out the importance of not only considering magnitude and hypocentral distance of the earthquakes to interpret dynamic triggering events but also directivity and wave mode effects.

Our numerical study shows that, for a given seismic strain amplitude, frequency, and direction of wave propagation, larger viscous shear stress is expected for more viscous fluids, stiffer background rocks, and thiner fractures. In other words, we showed that higher viscous shear stresses are expected for higher ratios f/f_{FF-FPD}, where f is the seismic wave frequency and f_{FF-FPD} is the frequency at which the fluid pressure gradient between the more compressed fracture and the connected (and less compressed) fracture produces maximal seismic attenuation. This implies that regions where pore fluids change or with different pressure and temperature conditions may experience more fracture unclogging, and consequently stronger permeability enhancement, than others. We showed that seismic attenuation may be a valuable attribute to characterize regions that are more affected by fracture unclogging.

We have also analyzed the importance of the fracture network distribution on the development of strong viscous shearing. We showed that for isotropic fracture distributions having the same fracture density, viscous shear stresses are more significant in fracture networks with a higher characteristic fracture length. This is related to both the increased likelihood of fracture connections, and hence of the pore fluid volume involved in the FPD process, and also to the fact that the FPD characteristic frequency is closer to the frequency of seismic waves. Finally, we found that the fracture aperture distribution also controls the development of viscous shear stresses. Spatially heterogeneous fracture apertures can produce locally enhanced viscous shear stress, which tend to be more pronounced for correlated fractures.

7 Appendix A: Mathematical formulation

The methodology used for this work is based a numerical solution of a coupled system of equations consisting of the linearized Navier-Stokes equation for the laminar flow of a compressible viscous fluid and the linear elastic equation for a nonporous solid material (Quintal et al., 2016). The coupled system of equations can be found by solving the conservation of momentum

$$\nabla \cdot \boldsymbol{\sigma} = 0, \tag{5}$$

where $\boldsymbol{\sigma}$ is the stress tensor whose components σ_{ij} are defined through generalized stress-strain relations in frequency domain

$$\sigma_{ij} = 2\mu\varepsilon_{ij} + \lambda e\delta_{ij} + 2i\omega\eta\varepsilon_{ij} + i\omega\eta_\lambda e\delta_{ij}, \tag{6}$$

with μ being the shear modulus of the material, η and η_K the shear and bulk viscosities, respectively, ω is the angular frequency and

$$\begin{aligned} \varepsilon_{ij} &= \frac{1}{2}\left(\frac{\partial u_i}{\partial x_j} + \frac{\partial u_j}{\partial x_i}\right), \\ e &= \sum_{i=1}^{3} \varepsilon_{ii}, \\ \lambda &= K - \frac{2}{3}\mu, \\ \eta_\lambda &= \eta_K - \frac{2}{3}\eta, \end{aligned} \tag{7}$$

where K is the bulk modulus of the material, u describes either the displacement of the fluid or that of the solid in the corresponding subdomains, and $i, j = x, y, z$. In the non-porous background, $\eta = \eta_K = 0$ and Eq. 6 reduces to the classical Hooke's law in an elastic material

$$\sigma_{ij} = 2\mu\varepsilon_{ij} + \lambda e\delta_{ij}. \tag{8}$$

Assuming that a compressible viscous fluid is filling the fractures, and hence $\mu = \eta_K = 0$, Eq. 6 in the fractures reduces to

$$\sigma_{ij} = Ke\delta_{ij} + 2i\omega\eta\varepsilon_{ij} - \frac{2}{3}i\omega\eta e\delta_{ij}. \tag{9}$$

The bulk viscosity of the fluid is set to zero under the assumption of quasistatic flow. As pointed out by Quintal et al. (2016), this means that in the fracture we solve the quasi-static (inertial terms neglected) linearized (advective acceleration neglected) Navier-Stokes equations for the laminar flow of a Newtonian fluid (Zimmerman & Main, 2004). Consequently, the viscous shear stresses can only be caused by fluid pressure diffusion inside the hydraulically connected fractures. This approach is relevant for lithologies with low permeability such as those prevailing in Enhanced Geothermal Systems in which hydraulically fracturing the host rock is crucial for the economic exploitation of geothermal resources. The hydraulic response of such low-permeability crystalline rocks containing fractures should be particularly susceptible to unclogging because small changes in the flow paths may have large impacts on effective permeability (Manga et al., 2012). Finally, in the frequency domain, the viscous shear stress in Eq. 1 can be written as

$$\tau_{ij}(\omega) = \eta i\omega\left(\frac{\partial u_i}{\partial x_j} + \frac{\partial u_j}{\partial x_i}\right), \qquad i,j = x,y,z, \tag{10}$$

which is zero in the nonporous background.

Acknowledgments

This work was supported by a grant from the Swiss National Science Foundation (GENERATE, Grant number 166900) and completed within the SCCER-SOE framework. The authors gratefully acknowledge comments and suggestions from Rälf Janicke and an anonymous reviewer. The data for this paper are available at `https://doi.org/10.5281/zenodo.3404067`.

References

Amann, F., Gischig, V., Evans, K., Doetsch, J., Jalali, R., Valley, B., ... Giardini, D. (2018). The seismo-hydromechanical behavior during deep geothermal reservoir stimulations: open questions tackled in a decameter-scale in situ stimulation experiment. *Solid Earth*, *9*(1), 115–137.

Ameli, P., Elkhoury, J. E., Morris, J. P., & Detwiler, R. L. (2014). Fracture permeability alteration due to chemical and mechanical processes: a coupled high-resolution model. *Rock mechanics and rock engineering*, *47*(5), 1563–1573.

Bai, R., & Tien, C. (1997). Particle detachment in deep bed filtration. *Journal of colloid and interface science*, *186*(2), 307–317.

Bakulin, A., Grechka, V., & Tsvankin, I. (2000). Estimation of fracture parameters from reflection seismic data-part I: HTI model due to a single fracture set. *Geophysics*, *65*(6), 1788–1802.

Beresnev, I. A., & Johnson, P. A. (1994). Elastic-wave stimulation of oil production: A review of methods and results. *Geophysics*, *59*(6), 1000–1017.

Bergendahl, J., & Grasso, D. (2000). Prediction of colloid detachment in a model porous media: Hydrodynamics. *Chemical Engineering Science*, *55*(9), 1523–1532.

Borg, I., Stone, R., Levy, H., & Ramspott, L. (1976). *Information pertinent to the migration of radionuclides in ground water at the nevada test site. part 1. review and analysis of existing information* (Tech. Rep.). California Univ.

Brodsky, E. E., & Prejean, S. G. (2005). New constraints on mechanisms of remotely triggered seismicity at long valley caldera. *Journal of Geophysical Research: Solid Earth*, *110*(B4).

Brodsky, E. E., Roeloffs, E., Woodcock, D., Gall, I., & Manga, M. (2003). A mechanism for sustained groundwater pressure changes induced by distant earthquakes. *Journal of Geophysical Research: Solid Earth*, *108*(B8).

Candela, T., Brodsky, E. E., Marone, C., & Elsworth, D. (2014). Laboratory evidence for particle mobilization as a mechanism for permeability enhancement via dynamic stressing. *Earth and Planetary Science Letters*, *392*, 279–291.

Candela, T., Brodsky, E. E., Marone, C., & Elsworth, D. (2015). Flow rate dictates permeability enhancement during fluid pressure oscillations in laboratory experiments. *Journal of Geophysical Research: Solid Earth*, *120*(4), 2037–2055.

Carcione, J. M. (2007). *Wave fields in real media: Wave propagation in anisotropic, anelastic, porous and electromagnetic media* (Vol. 38). Elsevier.

Chen, X., Wu, Z., Cai, Q., & Cao, W. (2018). Effect of ultrasonic stimulation on particle transport and fate over different lengths of porous media. *Journal of hydrology*, *559*, 972–983.

de Dreuzy, J.-R., Davy, P., & Bour, O. (2001). Hydraulic properties of two-dimensional random fracture networks following a power law length distribution: 1. effective connectivity. *Water Resources Research*, *37*(8), 2065–2078.

Degueldre, C., Baeyens, B., Goerlich, W., Riga, J., Verbist, J., & Stadelmann, P. (1989). Colloids in water from a subsurface fracture in granitic rock, grimsel test site, switzerland. *Geochimica et Cosmochimica Acta*, *53*(3), 603–610.

Economides, M. J., & Nolte, K. G. (1989). *Reservoir stimulation* (Vol. 2). Prentice Hall Englewood Cliffs, NJ.

Elkhoury, J. E., Brodsky, E. E., & Agnew, D. C. (2006). Seismic waves increase permeability. *Nature*, *441*(7097), 1135.

Elkhoury, J. E., Niemeijer, A., Brodsky, E. E., & Marone, C. (2011). Laboratory observations of permeability enhancement by fluid pressure oscillation of in situ fractured rock. *Journal of Geophysical Research: Solid Earth*, *116*(B2).

Faoro, I., Elsworth, D., & Marone, C. (2012). Permeability evolution during dynamic stressing of dual permeability media. *Journal of Geophysical Research: Solid Earth*, *117*(B1).

Farías, C., Lupi, M., Fuchs, F., & Miller, S. A. (2014). Seismic activity of the nevados de chillán volcanic complex after the 2010 mw8. 8 maule, chile, earthquake. *Journal of Volcanology and Geothermal Research*, *283*, 116–126.

Guo, J., Rubino, J. G., Glubokovskikh, S., & Gurevich, B. (2017). Effects of fracture intersections on seismic dispersion: theoretical predictions versus numerical simulations. *Geophysical Prospecting*, *65*(5), 1264–1276.

Hill, D. P. (2008). Dynamic stresses, coulomb failure, and remote triggering. *Bulletin of the Seismological Society of America*, *98*(1), 66–92.

Hunziker, J., Favino, M., Caspari, E., Quintal, B., Rubino, J. G., Krause, R., & Holliger, K. (2018). Seismic attenuation and stiffness modulus dispersion in porous rocks containing stochastic fracture networks. *Journal of Geophysical Research: Solid Earth*.

Ishibashi, T., Elsworth, D., Fang, Y., Riviere, J., Madara, B., Asanuma, H., ... Marone, C. (2018). Friction-stability-permeability evolution of a fracture in granite. *Water Resources Research*, *54*(12), 9901–9918.

Karve, P. M., Fathi, A., Poursartip, B., & Kallivokas, L. F. (2017). Source parameter inversion for wave energy focusing to a target inclusion embedded in a three-dimensional heterogeneous halfspace. *International Journal for Numerical and Analytical Methods in Geomechanics*, *41*(7), 1016–1037.

Kocharyan, G., Vinogradov, E., Gorbunova, E., Markov, V., Markov, D., & Pernik, L. (2011). Hydrologic response of underground reservoirs to seismic vibrations. *Izvestiya, Physics of the Solid Earth*, *47*(12), 1071–1082.

Kutay, M. E., & Aydilek, A. H. (2009). Pore pressure and viscous shear stress distribution due to water flow within asphalt pore structure. *Computer-Aided Civil and Infrastructure Engineering*, *24*(3), 212–224.

Li, X., Zhang, P., Lin, C., & Johnson, W. P. (2005). Role of hydrodynamic drag on microsphere deposition and re-entrainment in porous media under unfavorable conditions. *Environmental science & technology*, *39*(11), 4012–4020.

Lissa, S., Barbosa, N. D., Rubino, J. G., & Quintal, B. (2019). Seismic attenuation and dispersion in poroelastic media with fractures of variable aperture distributions. *Solid Earth*, *10*, 1321–1336.

Liu, W., & Manga, M. (2009). Changes in permeability caused by dynamic stresses in fractured sandstone. *Geophysical Research Letters*, *36*(20).

Lupi, M., Frehner, M., Weis, P., Skelton, A., Saenger, E. H., Tisato, N., ... Driesner, T. (2017). Regional earthquakes followed by delayed ground uplifts at campi flegrei caldera, italy: Arguments for a causal link. *Earth and Planetary Science Letters*, *474*, 436–446.

Lupi, M., Fuchs, F., & Saenger, E. H. (2017). Numerical simulations of passing seismic waves at the larderello-travale geothermal field, italy. *Geophysical Research Letters*, *44*(11), 5418–5426.

Lupi, M., Ricci, B. S., Kenkel, J., Ricci, T., Fuchs, F., Miller, S. A., & Kemna, A. (2015). Subsurface fluid distribution and possible seismic precursory signal at the salse di nirano mud volcanic field, italy. *Geophysical Journal International*, *204*(2), 907–917.

Lupi, M., Saenger, E. H., Fuchs, F., & Miller, S. (2013). Lusi mud eruption triggered by geometric focusing of seismic waves. *Nature Geoscience*, *6*(8), 642.

Manga, M., Beresnev, I., Brodsky, E. E., Elkhoury, J. E., Elsworth, D., Ingebritsen, S. E., ... Wang, C.-Y. (2012). Changes in permeability caused by transient stresses: Field observations, experiments, and mechanisms. *Reviews of geophysics*, *50*(2).

Manga, M., & Brodsky, E. (2006). Seismic triggering of eruptions in the far field: Volcanoes and geysers. *Annu. Rev. Earth Planet. Sci*, *34*, 263–291.

Manga, M., Brodsky, E. E., & Boone, M. (2003). Response of streamflow to multiple earthquakes. *Geophysical Research Letters*, *30*(5).

Mirzaei-Paiaman, A., & Nourani, M. (2012). Positive effect of earthquake waves on well productivity: Case study: Iranian carbonate gas condensate reservoir. *Scientia Iranica*, *19*(6), 1601–1607.

Mogi, K., Mochizuki, H., & Kurokawa, Y. (1989). Temperature changes in an artesian spring at usami in the izu peninsula (japan) and their relation to earthquakes. *Tectonophysics*, *159*(1-2), 95–108.

Nolte, D., & Pyrak-Nolte, L. (1991). Stratified continuum percolation: Scaling geometry of hierarchical cascades. *Physical Review A*, *44*(10), 6320.

Pride, S. R., Flekkøy, E. G., & Aursjø, O. (2008). Seismic stimulation for enhanced oil recovery. *Geophysics*, *73*(5), O23–O35.

Pyrak-Nolte, L. J., & Morris, J. (2000). Single fractures under normal stress: The relation between fracture specific stiffness and fluid flow. *International Journal of Rock Mechanics and Mining Sciences*, *37*(1-2), 245–262.

Pyrak-Nolte, L. J., & Nolte, D. D. (2016). Approaching a universal scaling relationship between fracture stiffness and fluid flow. *Nature communications*, *7*, 10663.

Quintal, B., Rubino, J. G., Caspari, E., & Holliger, K. (2016). A simple hydromechanical approach for simulating squirt-type flow. *Geophysics*, *81*(4), D335–D344.

Roberts, P. M. (2005). Laboratory observations of altered porous fluid flow behavior in berea sandstone induced by low-frequency dynamic stress stimulation. *Acoustical Physics*, *51*(1), S140–S148.

Roberts, P. M., & Abdel-Fattah, A. I. (2009). Seismic stress stimulation mobilizes colloids trapped in a porous rock. *Earth and Planetary Science Letters*, *284*(3-4), 538–543.

Rojstaczer, S., Wolf, S., & Michel, R. (1995). Permeability enhancement in the shallow crust as a cause of earthquake-induced hydrological changes. *Nature*, *373*(6511), 237.

Rubino, J. G., Caspari, E., Müller, T. M., & Holliger, K. (2017). Fracture connectivity can reduce the velocity anisotropy of seismic waves. *Geophysical Journal International*, *210*(1), 223–227.

Rubino, J. G., Caspari, E., Müller, T. M., Milani, M., Barbosa, N. D., & Holliger, K. (2016). Numerical upscaling in 2-d heterogeneous poroelastic rocks: Anisotropic attenuation and dispersion of seismic waves. *Journal of Geophysical Research: Solid Earth*, *121*(9), 6698–6721.

Rubino, J. G., Guarracino, L., Müller, T. M., & Holliger, K. (2013). Do seismic waves sense fracture connectivity?. *Geophysical Research Letters*, *40*(4), 692–696.

Rubino, J. G., Müller, T. M., Guarracino, L., Milani, M., & Holliger, K. (2014). Seismoacoustic signatures of fracture connectivity. *Journal of Geophysical Research: Solid Earth*, *119*(3), 2252–2271.

Rudolph, M., & Manga, M. (2010). Mud volcano response to the 4 april 2010 el mayor-cucapah earthquake. *Journal of Geophysical Research: Solid Earth*, *115*(B12).

Saccorotti, G., Piccinini, D., Mazzarini, F., & Zupo, M. (2013). Remotely triggered micro-earthquakes in the larderello-travale geothermal field (italy) following the 2012 may 20, mw 5.9 po-plain earthquake. *Geophysical Research Letters*, *40*(5), 835–840.

Shi, Y., Liao, X., Zhang, D., & Liu, C.-p. (2019). Seismic waves could decrease the permeability of the shallow crust. *Geophysical Research Letters*.

Taira, T., Nayak, A., Brenguier, F., & Manga, M. (2018). Monitoring reservoir response to earthquakes and fluid extraction, salton sea geothermal field, california. *Science Advances*, *4*(1), e1701536.

Wang, C.-Y. (2007). Liquefaction beyond the near field. *Seismological Research Letters*, *78*(5), 512–517.

Wang, C.-y., Chia, Y., Wang, P.-l., & Dreger, D. (2009). Role of s waves and love waves in coseismic permeability enhancement. *Geophysical Research Letters*, *36*(9).

Weaver, K., Cox, S., Townend, J., Rutter, H., Hamling, I., & Holden, C. (2019). Seismological and hydrogeological controls on new zealand-wide groundwater level changes induced by the 2016 mw 7.8 kaikōura earthquake. *Geofluids*.

Xue, L., Li, H.-B., Brodsky, E. E., Xu, Z.-Q., Kano, Y., Wang, H., … Zhang, W. (2013). Continuous permeability measurements record healing inside the wenchuan earthquake fault zone. *Science*, *340*(6140), 1555–1559.

Zhang, W., Tang, X., Weisbrod, N., & Guan, Z. (2012). A review of colloid transport in fractured rocks. *Journal of Mountain Science*, *9*(6), 770–787.

Zhang, Y., Fu, L.-Y., Huang, F., & Chen, X. (2015). Coseismic water-level changes in a well induced by teleseismic waves from three large earthquakes. *Tectonophysics*, *651*, 232–241.

Zimmerman, R., & Main, I. (2004). Hydromechanical behavior of fractured rocks. *International Geophysics Series*, *89*, 363–422.